

Sizes, Shapes, and Correlations of Lyman Alpha Clouds and Their Evolution in the CDM+ Λ Universe

Renyue Cen^{1,2} and Robert A. Simcoe¹

Email: (cen,rasimcoe)@astro.princeton.edu

Received _____; accepted _____

¹Princeton University Observatory, Princeton University, Princeton, NJ 08544

²Department of Astronomy, University of Washington, Seattle, WA 98195

ABSTRACT

This study analyzes the sizes, shapes and correlations of Ly α clouds produced by a hydrodynamic simulation of a spatially flat CDM universe with a non-zero cosmological constant ($\Omega_0 = 0.4$, $\Lambda_0 = 0.6$, $\sigma_8 = 0.79$), over the redshift range $2 \leq z \leq 4$. The Ly α clouds range in size from several kiloparsecs to about a hundred kiloparsecs in proper units, and they range in shape from roundish, high column density regions with $N_{HI} \geq 10^{15} \text{ cm}^{-2}$ to low column density sheet-like structures with $N_{HI} \leq 10^{13} \text{ cm}^{-2}$ at $z=3$. The most common shape found in the simulation resembles that of a flattened cigar. The physical size of a typical cloud grows with time roughly as $(1 + z)^{-3/2}$ while its shape hardly evolves (except for the most dense regions $\rho_{cut} > 30$). Our result indicates that any simple model with a population of spheres (or other shapes) of a uniform size is oversimplified; if such a model agrees with observational evidence, it is probably only by coincidence. We also illustrate why the use of double quasar sightlines to set lower limits on cloud sizes is useful only when the perpendicular sightline separation is small ($\Delta r \leq 50h^{-1}\text{kpc}$). Finally, we conjecture that high column density Ly α clouds ($N_{HI} \geq 10^{15}\text{cm}^{-2}$) may be the progenitors of the lower redshift faint blue galaxies. This seems plausible because their correlation length, number density (extrapolated to lower redshift) and their masses are in fair agreement with those observed.

Subject headings: Cosmology: large-scale structure of Universe – cosmology: theory – intergalactic medium – quasars: absorption lines – hydrodynamics

1. Introduction

Acceptable theories of structure formation are those whose parameters have been tuned to match the most up-to-date cosmological observations. At high redshift, the current leading constraint on models is the data from COBE (Smoot et al. 1992), which fixes the amplitude of the power spectrum on very large scales ($\sim 1000h^{-1}\text{Mpc}$) to an accuracy of about 12%. At low (essentially zero) redshift, we demand that models fit current observations of our local universe, primarily those concerning the distributions of galaxies in (\vec{x}, \vec{v}) space. These include the abundance of clusters of galaxies, which fixes the amplitude of the power spectrum on scales of $\sim 8h^{-1}\text{Mpc}$ to about 10% accuracy (Bahcall & Cen 1992; Oukbir & Blanchard 1992; Bahcall & Cen 1993; White et al. 1993a; Viana & Liddle 1995; Bond & Myers 1996; Eke, Cole, & Frenk 1996; Pen 1996), the power spectrum of galaxies, which constrains the shape of the power spectrum on the intermediate-to-large scale of $\sim 10 - 100h^{-1}\text{Mpc}$ (Peacock & Dodds 1994; Feldman, Kaiser & Peacock 1994), the ratio of gas to total matter in galaxy clusters, which determines Ω_b/Ω_{tot} (White et al. 1993b). In addition, the current measurements of the Hubble constant (Fukugita, Hogan, & Peebles 1993; Freedman et al. 1994; Riess, Press, & Kirshner 1995; Hamuy et al. 1995) and the age constraint from the oldest globular clusters (Bolte & Hogan 1995) limit the range for H_o and the combination of Ω_0 and Λ_0 .

This observational suite has been examined by Ostriker & Steinhardt (1995) to constrain flat cold dark matter models with a non-zero cosmological constant (Peebles 1984; Efstathiou, Bond, & White 1992; Bahcall & Cen 1992; Kofman, Gnedin, & Bahcall 1993; Cen, Gnedin, & Ostriker 1993). The exercise is repeatable for other models (not necessarily flat) including the tilted cold dark matter model (Cen et al. 1992; Liddle, Lyth, & Sutherland 1992; Lidsey & Coles 1992; Adams et al. 1993; Lucchin, Matarrese, & Mollerach 1993), the mixed dark matter model (Davis, Summers & Schlegel 1992; Taylor

& Rowan-Robinson 1992; Klypin et al. 1993; Cen & Ostriker 1994; Ma & Bertschinger 1994), the open cold dark matter model (Gott 1982; Bucher, Goldhaber, & Turok 1995) and the primeval isocurvature baryon model (Peebles 1987a,b; Cen, Ostriker, & Peebles 1993). The allowed parameter space for the family of Gaussian cosmological models with the tunable parameters (H_o , Ω_0 , Λ_0 , $R_{H/C}$, n , ISO, ADIA) is thus quite limited. In this context, H_o , Ω_0 , and Λ_0 are the Hubble constant, the density parameter, and the value of cosmological constant, all in the present epoch. $R_{H/C}$ is the mass ratio of hot to cold matter, n is the asymptotic power spectral index on large scales, and ISO and ADIA denote isocurvature and adiabatic models. Although it is possible to further tighten this parameter space simply by making more accurate observations of the forementioned quantities, we should not overlook any other *independent* tests which could help to distinguish between contending models.

The Ly α forest lines observed in the spectra of high redshift quasars have two unique qualities which distinguish them from other observationally accessible phenomena, at redshifts between the epoch observed by COBE and our local universe. First, each line of sight indiscriminately samples the distribution of neutral hydrogen gas over a wide redshift range ($z \sim 0 - 5$) along random lines of sight (i.e., foreground objects are unrelated to the background quasar). Second, each individual spectrum contains a large amount of information about low absorption regions (e.g. voids, fluctuating Gunn-Peterson absorption) as well as information from high absorption “cloud” lines (number densities of clouds at different redshifts, b -parameters of the individual clouds, correlations of the clouds, relationship with other cosmic entities). With a database of thousands of observed quasars, the total amount of information available is very large, allowing for very detailed statistical studies (e.g., Carswell et al. 1991; Rauch et al. 1993; Petitjean et al. 1993; Schneider et al. 1993; Cristiani et al. 1995; Hu et al. 1995; Tytler et al. 1995). These facts, taken together, suggest that the Ly α forests constitute perhaps the most rich and unbiased

sample available for studying the universe at moderate redshift.

Recent cosmological hydrodynamic simulations by several independent groups have consistently shown that Ly α clouds are an integral part of the cosmic structure, resulting naturally from the gravitational growth and/or collapse of density fluctuations on small-to-intermediate scales of ~ 100 kpc to a few Mpc in comoving units (Cen et al. 1994, CMOR hereafter; Zhang et al. 1995; Hernquist et al. 1996). Several simple population models have been designed to examine the (local) physical as well as (global) statistical properties of Ly α clouds (Sargent et al. 1980; Ostriker & Ikeuchi 1983; Ikeuchi & Ostriker 1986; Bahcall & Spitzer 1969; Arons 1972; Rees 1986; Ikeuchi 1986; Bond, Szalay, & Silk 1988). One of the essential simplifications in almost all these models is to assume that individual Ly α clouds are spherical. While the clouds produced in the new simulations may have some physical properties in common with these simple models, a visual inspection of the new simulation results reveals that the Ly α absorbing structures resulting from small-to-intermediate scale structure formation at high redshift are *far from spherical*. Furthermore, they seem to have a wide range of sizes. We presented these results first in CMOR, and then in much more detail in Miralda-Escudé et al. (1996, MCOR hereafter). Here, we present a quantitative study of the topological aspects of the Ly α clouds, complementing the topics covered in CMOR and MCOR.

In the redshift range from two to four, Ly α clouds exhibit a rich spectrum of structure, ranging in shape from semi-spherical to filamentary and even sheet-like. The spherical structures often reside at density maxima (with $N_{HI} \geq 10^{15} \text{ cm}^{-2}$) located in the centers of extended structures, while the filaments and sheets tend to have a low N_{HI} ($\leq 10^{13} \text{ cm}^{-2}$), and form a web-like, interconnecting network covering large portion of the simulation box ($L = 10h^{-1}\text{Mpc}$ comoving).

We also show that it is not unusual for pairs of quasar sightlines to contain absorption

features at close wavelengths. In particular, we show that “common” absorption features (coincident lines) in sightline pairs separated by $100h^{-1}$ proper kpc or more are probably due to absorption by *different clouds*, while on separations smaller than $40h^{-1}$ kpc, double sightlines are mostly likely to actually pierce a common cloud.

Finally, we show that Ly α clouds are spatially significantly clustered, with a correlation length of roughly $1 - 2h^{-1}$ Mpc comoving (for the high column density clouds of $N_{HI} \geq 10^{15} \text{ cm}^{-2}$) at redshift $z \sim 0.5 - 1.0$. This suggests the possibility of an intriguing connection to faint blue objects (Koo 1986; Tyson 1988; Cowie et al. 1988).

This paper is organized as follows. Some brief descriptions of the simulations (for more details see MCOR) and our cloud identification method are presented in §2. Results and conclusions are given in §3 and §4.

2. Simulations and Cloud Identification

2.1. Simulations

We simulate the formation of Ly α clouds in a spatially flat cold dark matter universe with a cosmological constant (Λ CDM), using the following cosmological parameters: $H_0 = 65 \text{ km/s/Mpc}$, $\Omega_{0,CDM} = 0.3645$, $\Lambda_0 = 0.6$, $\Omega_{0,b} = 0.0355$ (cf. Walker et al. 1991), $\sigma_8 = 0.79$ (the simulations we use in this paper are the same as those used in CMOR and MCOR). The primary motivation for choosing this model is that it best fits the available observations which were summarized in the introduction. The simulation box size is $10h^{-1}$ comoving Mpc per side, and contains $N = 288^3$ cells and 144^3 dark matter particles. The cell size is $35 h^{-1}$ comoving kpc, corresponding to a average baryonic cell mass of $6.3 \times 10^5 M_\odot$, with the true spatial and mass resolutions being about 2 and 8 times worse than those values, respectively. At $z = 3$, the Jeans length, $\lambda_J \equiv (\pi c_s^2/G\bar{\rho}_{tot})^{1/2}$

for $c_s = v_{rms} = 10$ km/s, is equal to $400h^{-1}$ kpc in comoving units, or 11 cells. The power spectrum transfer function is computed using the method described in Cen, Gnedin, & Ostriker (1993). We use a new shock-capturing Total Variation Diminishing (TVD) cosmological hydrodynamic code described in Ryu et al. (1993).

All the atomic processes for a plasma of (H, He) of primeval composition (76%,24%) in mass are included, using the heating, cooling, and ionization terms described in Cen (1992). We calculate self-consistently the average background photoionizing radiation field as a function of frequency, assuming the radiation field is spatially uniform (i.e., optically thin). The evolution of the radiation field is calculated given the average attenuation in the simulated box and the emission (both from the gas itself and from the assumed sources of ionizing photons). The time-dependent equations for the ionization structure of the gas are solved by iteration using an implicit method, to avoid the instabilities that arise in solving stiff equations. In general, the abundances of different species are close to ionization equilibrium between recombination and photoionization after most of the gas has been photoionized.

We model galaxy formation as in Cen & Ostriker (1992, 1993a,b). The material turning into collisionless particles as “galaxies” is assumed to emit ionizing radiation, with two types of spectra: one characteristic of star formation regions and the other characteristic of quasars, with efficiencies (i.e., the fraction of rest-mass energy converted into radiation) of $e_{UV,*} = 5 \times 10^{-6}$, and $e_{UV,Q} = 6 \times 10^{-6}$, respectively. We adopt the emission spectrum of massive stars from Scalo (1986) and that of quasars from Edelson and Malkan (1986). Details of how we identify galaxy formation and follow the motions of formed galaxies have been described in Cen & Ostriker (1993a). Note that in this simulation supernova energy feedback into the intergalactic medium from aging massive stars is not included.

2.2. Ly α Cloud Identification

Perhaps the most critical decision which must be made in a study such as this is how to define a Ly α “cloud”. This is not as simple as it may seem, because the smooth transition in density between the global intergalactic medium and the local structures within it can blur the distinction between actual clouds and the intercloud medium. However, in order to examine the structure of Ly α clouds in any quantitative way, it is absolutely necessary to adopt some sort of definition of the boundary of a cloud. The simplest approach which we believe to be meaningful is to identify clouds as regions with densities above a chosen threshold.

There are two major motivations for defining our clouds in this manner. First of all, this method allows us to associate the clouds found at each density cut with a particular column density, once we obtain information about the characteristic sizes of the clouds. This is a desirable feature because we can only observe Ly α forest clouds through absorption lines in QSO spectra. Second, density perturbations with amplitudes larger than a certain threshold become self-gravitating, bound clouds. For a spherical cloud, the average overdensity at which a cloud breaks away from the general Hubble expansion and becomes self-gravitating is ~ 5.55 . Thus, our cloud definition also has physical motivation in that structures above some high density threshold are gravitationally bound, distinct systems. Having chosen a general strategy for defining our clouds, we now describe the details of the grouping procedure.

Cells with a baryonic density below a chosen value (3, 10, and 30 will be used) in units of the global mean of the baryonic density are cut out of the original density array. Then, clouds are defined by grouping the remaining cells using the DENMAX scheme (Bertschinger & Gelb 1991) as follows.

First, two sets of baryonic densities are stored. One is the original density output

array from the simulation (ρ_{org} , 288^3 elements), and the second is a smoothed version of ρ_{org} with a Gaussian smoothing window of radius 1.5 cells (ρ_{smooth} , 288^3 elements). The smoothing is performed to eliminate any small, cell-to-cell density fluctuations, which could be physical in the form of small discontinuities or oscillating sound waves, or just numerical noises. Such small-scale fluctuations could result in the identification of small unwanted clouds with sizes on the order of one cell. At the same time, since the true resolution of the simulation is close to 2-3 cells, a Gaussian smoothing window of radius 1.5 cells should preserve all information regarding “real” adjacent structures. A larger smoothing window could merge real and separate entities which are actually well-resolved in the simulation. We have made rather extensive experiments on the smoothing operation and conclude that the adopted smoothing window size is appropriate, as will be shown below.

After the smoothing operation is performed, we cut out all elements of ρ_{smooth} and ρ_{org} whose ρ_{org} values are below a chosen value, ρ_{cut} . We then collect the uncut cells of ρ_{org} (using the DENMAX scheme) by propagating each cell along the gradient of ρ_{smooth} until it reaches a local density maximum. All the cells collected at a particular local maximum are grouped into one “cloud”.

Once the cells have been grouped, we examine the shapes and sizes of the resultant “clouds” by approximating them as *ellipsoids*. A symmetric 3×3 moment tensor is created for each cloud of the form $T_{11} = \Delta x^2$; $T_{22} = \Delta y^2$; $T_{12} = \Delta x \Delta y$; and so on. This tensor is diagonalized, and the square roots of the eigenvalues yield the lengths of the semi-major and semi-minor axes, a', b', c' , in descending order of length. For cells where Δx , Δy , or $\Delta z = 0$, we account for the finite size of a single cell by finding $\frac{\int x^2 dy dx}{\int dy dx} = \frac{1}{12}$ for a 1 cell square and adding that to the tensor component for a particular cloud. This method underestimates the actual axial lengths of an ellipsoid, because it only computes moments. We attempt to correct this by scaling up the values of a', b' , and c' (determined above) by a factor of

$$\left(\frac{V}{4\pi a'b'c'/3}\right)^{1/3} : (a, b, c) = (a', b', c')\left(\frac{V}{4\pi a'b'c'/3}\right)^{1/3}, \quad (1)$$

where V is the actual volume of the cloud computed by summing over all the member cells of the cloud.

3. Results

3.1. A Visual Inspection

We first present a three dimensional visual description of the structure of the Ly α clouds produced in the simulation. Figures (1a,b,c) display the isodensity contour surfaces at $z = 3$ for $\rho_{cut} = (3, 10, 30)$, respectively. Here, ρ_{cut} is the baryonic density in units of its global mean. The box size is $10h^{-1}$ comoving Mpc. The most striking visual feature is the network of sheets and filaments spanning the box. In Figure 1a we see that most of the structures are connected over the entire box, and it is apparent that most of the covering areas [i.e., cross section for quasar lines of sight at low column densities ($\leq 10^{13} \text{ cm}^{-2}$; see below)] are sheet-like objects. Although this result is for the particular Λ CDM universe simulated here, we expect this qualitative picture to be fairly generic for any CDM-like model (HDM-like models should show even more prominent sheets, while models like PBI are likely to be less coherent). At a higher density of $\rho_{cut} = 10$ (Figure 1b) most structures become filamentary and more isolated. When the isodensity reaches $\rho_{cut} = 30$ (Figure 1c), most of the filaments are replaced by relatively round systems, which are typically isolated with separations of about one comoving megaparsec.

The second noticeable visual feature is the existence of a large, low density region at the center of the box, occupying more than half of the simulation volume. Since the initial condition of the simulation is not constrained (i.e., it is only a random realization of the

cosmological model in such a volume), this void indicates that the simulation box may still not be large enough to contain a “fair” volume for the structures under consideration. It may be necessary to use a larger simulation box, perhaps $20 - 30h^{-1}\text{Mpc}$ on a side, in order to properly sample the objects in question. Different properties will be affected by the simulation volume to varied degrees. We expect that the most significant differences will be in quantities like void sizes, or correlations.

Let us now examine the individual clouds to assess the general accuracy of our grouping scheme. Figure 2a shows clouds at $\rho_{cut} = 3$ for two randomly selected slices of size $5 \times 5h^{-2}\text{Mpc}^2$ with thickness of $175h^{-1}\text{kpc}$ (all lengths are in comoving units) at $z = 3$. The two left panels show the density contours of levels $10^{(i-1)/2} \rho_{cut}$, $i = 1, 2, 3, \dots$, and the two right panels show the identified Ly α clouds in the same slices. Two symbols are used to show two types of clouds: the filled dots represent “large” clouds with the dot size roughly proportional to the actual size of the cloud, and the open circles are for the “small” clouds. A cloud is called “small” if its smallest axis does not exceed 3 cells in length, and “large” if it does. Figure 2b is similar to Figure 2a, but with $\rho_{cut} = 10$, and for two different slices. We note that “large” clouds are typically embedded in larger, extended density structures while “small” ones are more isolated. A close, one-by-one examination of the density maxima in the density contour plots indicates that each identified cloud corresponds to a well defined density maximum (Some clouds, especially “small” ones, have no corresponding density maxima simply because their densities fall below the contour levels when averaged over the slice thickness to be displayed). It appears that our smoothing operation and cloud identification scheme indeed yield well defined, distinct clouds with one particularly desirable feature: they are neither over-merged in the sense that a single cloud contains multiple structures of comparable size (over-smoothed), nor over-separated in the sense that artificial clouds are created by small-scale small-amplitude density fluctuations (undersmoothed).

When the clouds are classified into “large” and “small” groups, we find that most of the clouds are “small”: the fraction of “small” clouds at $\rho_{cut} = (3, 10, 30)$ at $z = 3$ is (62%, 92%, 98%), containing (14%, 49%, 63%) of the total cloud mass. The fact that a large fraction of the baryonic mass is in “small” clouds indicates that a *higher resolution simulation is perhaps needed* before we can be absolutely sure that these clouds are resolved properly. Inclusion of more initial small scale power, which is limited by the Nyquist frequency of a simulation, might further increase the fraction of “small” clouds.

We note in passing that we also experimented with the conventional friends-of-friends grouping algorithm, with a linking length of one cell. The resulting clouds were obviously not useful for our analyses. For example, at $\rho_{cut} = 3$, most of the volume, as well as mass, wound up in a single supercloud because the distinct clouds as shown in Figure 2 were linked together by touching boundaries. In other words, the friends-of-friends grouping scheme picks out large, inter-connected networks (see Figure 1a) but not the individual structures embedded within them.

3.2. Quantitative Measures

We have chosen to focus on three quantitative aspects of the identified Ly α clouds: their sizes, shapes, and correlations. In addition, double quasar sightline analysis is performed.

To facilitate quantitative discussions, we relate the mass density of a cloud to its column density. Assuming that the clouds are in photoionization equilibrium, the column density of a cloud can be related to the parallel size and density of the cloud (assuming that the density is uniform across the cloud along the line of sight) as

$$N_H = 8.18 \times 10^{11} \left(\frac{\Omega_b}{0.0125 h^{-2}} \right)^2 \left(\frac{j_{HI}}{10^{-12}} \right)^{-1} \left(\frac{T}{10^4} \right)^{-0.7} \frac{L}{100 kpc} \left(\frac{\rho_{cut}}{\langle \rho_b \rangle} \right)^2 \left(\frac{1+z}{4} \right)^6 \text{ cm}^{-2}, \quad (2)$$

where Ω_b is the baryonic density parameter, T the temperature in Kelvin, j_{HI} the hydrogen photoionization rate, ρ_b and $\langle \rho_b \rangle$ the baryonic density of the cloud and the mean baryonic density at the redshift in question, L the proper size of the cloud along the line of sight, and z the redshift. For a photoionization radiation field with power-law form ν^{-1} , $j_{HI} = 4.34 \times 10^{-12} J_{LL} \text{ sec}^{-1}$, where J_{LL} is the intensity of the photoionization field at the Lyman limit in the usual units ($10^{-21} \text{ erg/cm}^2/\text{hz/sec/sr}$). Taking $\Omega_b = 0.0125h^{-2}$, $j_{HI} = 7.0 \times 10^{-13} \text{ sec}^{-1}$, $T = 2 \times 10^4$ Kelvin, $L = 40$ kpc as typical values at $z = 3$, one finds that $N_{HI} = (2.5 \times 10^{12}, 2.7 \times 10^{13}, 2.5 \times 10^{14}) \text{ cm}^{-2}$ for $\rho_{cut} = (3, 10, 30)$. Of course, exact column densities would depend on exact values of the assumed quantities as well as the actual density distribution. We expect that the actual density distribution, which is non-uniform, will increase the column densities. For example, redistribution of the same mass within L into a (one dimensional) coreless, non-uniform one would result in a column density $(1 + \alpha)^2 / (1 + 2\alpha)$ times that of the uniform density distribution, where α is the slope of the density profile. We simply increase the above estimates by a factor of four to account for the gradient in the density distribution of a cloud [note that this factor of four is fairly plausible for a reasonable α ($\sim -1/2$) in the one dimensional singular case or a relatively lower α value for a non-singular profile. We also note that this factor of four can also be achieved if Ω_b is twice the value adopted here, in the light of recent new measurements on the deuterium abundance (Tytler, Fan, & Burles 1996)], thus obtaining

$$N_{HI} = (1.0 \times 10^{13}, 1.1 \times 10^{14}, 1.0 \times 10^{15}) \text{ cm}^{-2} \quad \text{for } \rho_{cut} = (3, 10, 30) \quad \text{at } z = 3. \quad (3)$$

We will use the above relation for quantitative discussions.

3.2.1. A Few Simple Global Quantities

Before engaging in a more detailed quantitative discussion of cloud properties, we present a few simple, global quantities. Listed in Table 1 are the numbers of clouds at

each redshift and density threshold, the baryonic mass fraction of such clouds, the mean inter-cloud separation in proper units, and the mean cloud mass. Two points are interesting. First, while the average cloud increases its mass by a factor of about $3 - 4$ from $z = 4$ to $z = 2$, the number of clouds decreases by a factor two. This indicates that the merging of old clouds and creation of new clouds are of comparable importance. Second, the fraction of baryonic mass contained in Ly α clouds is large. For example, at redshifts (2,3,4), (31%, 29%, 26%) of baryons are found in regions with densities between $\rho_{cut} = 3$ and $\rho_{cut} = 30$ (i.e., $N_{HI} \sim 10^{13} - 10^{15} \text{ cm}^{-2}$).

3.2.2. Sizes of Ly α Clouds

We define the characteristic “size” of a cloud as

$$S \equiv (abc)^{1/3}, \quad (4)$$

where a , b , and c are the semi-axes of the ellipsoid approximating the cloud, measured in proper physical units (see §2.2 for definition of a, b, c). For a true ellipsoid cloud, the volume is $V = \frac{4\pi}{3}S^3$.

Figure 3 shows the cumulative distribution of cloud sizes at $z = 3$ for $\rho_{cut} = (3, 10, 30)$, respectively. The thin curves are weighted by A , where

$$A \equiv ab + ac + bc, \quad (5)$$

and the thick curves are weighted by mass. A is an approximation of the average covering area of a cloud on the sky, which is proportional to the probability of the cloud intersecting a line of sight. The A -weighted and mass-weighted distributions are very similar, implying that A and mass are correlated. Clouds are larger at lower ρ_{cut} , as expected, and they

exhibit a wide range in size, from a few to about a hundred proper kiloparsecs. The median size varies from $15h^{-1}$ kpc at $\rho_{cut} = 30$ to $35h^{-1}$ kpc for $\rho_{cut} = 3$. Note that S is only the cube root of the effective volume of a cloud, so the distribution of cloud sizes would be more varied, if we used a (semi-major axis of an ellipsoid) instead of S as a measure of size.

Figure 4 shows the redshift evolution of the median size of the Ly α clouds. Note that here the size (vertical axis) is in comoving length units, which might be easier to interpret. Our data indicates that Ly α clouds grow with time in comoving length units at a moderate rate, and that this rate depends *weakly* on the density (i.e., three curves for the three density cases are almost parallel to each other). The fact that denser regions are not shrinking, but rather expanding at a rate similar to that of less dense regions implies that the merger/accretion rate is *higher* in the dense regions than in less dense regions. Without merger/accretion effects, the high density regions would appear to shrink due to gravitational collapse.

To summarize, we find that Ly α clouds exhibit a wide range of sizes from a few proper kiloparsecs to about a hundred proper kiloparsecs at $z=3$. The comoving size of these clouds tends to increase slowly with time, implying that the proper physical size increases with time more rapidly than $(1 + z)^{-1}$.

3.2.3. *Shapes of Ly α Clouds*

Figures (5a,b,c) show the distributions of cloud shapes in the c/b - b/a plane for clouds at $\rho_{cut} = (3, 10, 30)$ at $z = 3$. Each dot represents one cloud and the contours indicate the density of clouds (weighted by A) in the plane. The contour levels are incremented up linearly from outside to inside. We see that the most common cloud at $\rho_{cut} = 3$ and 10 is an ellipsoid with axial ratios of $\sim 1 : 2 : 4$. However, at $\rho = 30$

the situation is interestingly different. Two major concentrations of clouds are seen at $(b/a, c/b) = (0.35, 0.85)$ and $(0.75, 0.85)$, indicating the existence of two distinct populations: filaments and near-spherical ellipsoids.

In order to conveniently show the evolution of shapes of the clouds and to relate shapes to other quantities, we define a simple “shape” parameter of a cloud as

$$\eta \equiv \frac{b^2 + c^2}{a^2}. \quad (6)$$

For an ideal (spherical, filamentary, disk) cloud, $\eta = (2, 0, 1)$. Some degeneracy exists for any value of η with such a simple definition. For example, $(a, b, c) = (1, 1, 0)$ and $(a, b, c) = (1, 1/\sqrt{2}, 1/\sqrt{2})$ both give $\eta = 1$.

Figure 6 shows η as a function of size S at $z = 3$ for $\rho_{cut} = (3, 10, 30)$. There is a trend, albeit with a large scatter, that larger clouds tend to be less spherical.

Figure 7 represents the A -weighted cumulative distribution of η for three cases at $z = 3$. We note two points. First, we see that there is negligibly small fraction of clouds with the shape parameter η greater 1.5, indicating that spherical clouds ($\eta = 2$) contribute only a tiny percentage to the total covering area of the clouds at all three density cuts. Second, we find a larger fraction of round clouds (large η) and filamentary clouds (η close to zero) at high densities than at a lower densities. This is due to the fact that the large sheets and filaments present at lower densities are broken up into both filaments and turn into roundish regions at higher densities, respectively. This quantitative result is consistent with the visual impression that structures go from sheets to filaments and spheres as the density goes from low to high (Figure 1). The fact that there are more filaments than spheres at all densities is probably a consequence of nonlinear evolution coupled with hydrodynamic (pressure) effects. The situation for dark halos might be different, since dark

matter distributions tend to be more unstable in lower dimensional structures.

Finally, we show in Figure 8 the redshift evolution of the median shape parameter η_{med} . It indicates that at $\rho_{cut} = 3$ the median shape of the clouds do not change with time, while at $\rho_{cut} = 30$ the clouds progress toward the shape of spheres (larger η) in time with a dramatic upturn from $z = 3$ to $z = 2$, possibly related to the collapse/merging of gas along the longest axis. The situation at the intermediate $\rho_{cut} = 10$ is between the above two cases.

In summary, we have shown that Ly α clouds display a variety of shapes ranging from semi-spherical clouds to filaments and sheets, with the most common shape being a “flattened cigar” with an axial ratio of $\sim 1 : 2 : 4$ at column density of $10^{13} - 10^{14} \text{ cm}^{-2}$, and being either a thin cigar with an axial ratios of $(1 : 3 : 3.4)$ or near sphere with an axial ratios of $(1 : 1.3 : 1.5)$ at column density of $> 10^{15} \text{ cm}^{-2}$. Larger clouds tend to be less spherical. The shapes of clouds with densities a few times the mean density of the universe evolve very weakly with time, whereas the clouds at higher densities ($\rho_{cut} \geq 30$) grow more spherical with time.

3.2.4. Double Quasar Line of Sight Analysis

None of our analyses so far have been directly comparable with observables. Here we attempt to project our theoretical models onto the observational plane. CMOR and MCOR have examined many of the properties of these clouds in detail, and found that the simulation results match observations fairly well. Here, we focus on the observations of double quasar sightlines (Smette et al. 1992; Dinshaw et al. 1994; Dinshaw et al. 1995; Smette et al. 1995; Fang et al. 1996; Bechtold & Yee 1996). Let us first describe our procedure for modeling these observations.

1. Once three dimensional clouds in the simulation box are identified (see §2.2), each

cell is labelled with an integer n , meaning that it belongs to cloud n (if n is zero, it means that the cell does not belong to any cloud, i.e., its density is below ρ_{cut}).

2. A random pair of sightlines separated by Δr is selected. Since the simulation box has no preferred orientation, we simply choose a direction perpendicular to one of three faces of the simulation box as the direction for the double sightlines.

3. Along each of the two sightlines we identify cells whose labels n (see Step 1) are non-zero, and then separate regions of different n into separate clouds, which we call Clouds-Along-Line-Of-Sight (CALOS’s). Note that each CALOS inherits its 3-d parent cloud label n .

4. We define the location of each CALOS in z -space by finding the ρ_{gas}^2 weighted center of the CALOS cells located along the sightline.

5. For each CALOS along sightline #1, if a CALOS within a velocity space separation D along the sightline #2 is found, the following operation is performed: an integer counter $N_{co,common}$ is incremented if the two CALOS’s share the same n , i.e., they belong to the same 3-d cloud. Otherwise an integer counter $N_{co,clustering}$ is incremented by 1. If both a common and a clustering line are found, we consider it to be a common pairing. The above exercise is repeated for each CALOS along sightline #2. We note that the bulk peculiar velocity of each CALOS is ignored in this calculation, i.e., the line-of-sight velocity difference between a pair of coincident lines simply reflects the line-of-sight real space distance difference. This should be a good approximation, because the peculiar velocity gradient is typically smaller than the Hubble constant on the scale D (see below) in which we are interested.

We perform this exercise on 10,000 randomly selected pairs of sightlines for each value of $\rho_{cut} = (3, 10, 30)$ at six different perpendicular separations, $\Delta r = (1, 3, 6, 12, 24, 48)$ cells. Figure 9 shows the fraction of lines which are coincident at $z = 3$, $N_{co,tot}/N_{tot}$, as a function

of Δr , where $N_{co,tot} = N_{co,common} + N_{co,clustering}$ and N_{tot} is total number of lines. Six curves are shown, corresponding to three values of $\rho_{cut} = (3, 10, 30)$, each at two values of $D = (50, 150)$ km/s. We see that *the line coincident rate decreases with increasing column density*. At a perpendicular proper separation of $100h^{-1}$ kpc and $\rho_{cut} = 3$ (corresponding to clouds with $N_{HI} = 10^{13}\text{cm}^{-2}$) about 1/2 to 3/4 of the sightlines should have coincident absorption features for $D = 50\text{km/s}$ to 150km/s . The line coincident rates drop to (27%, 38%) and (11%, 17%) for $\rho_{cut} = 10$ and $\rho_{cut} = 30$ (corresponding to clouds with $N_{HI} = 10^{14}\text{cm}^{-2}$ and $N_{HI} = 10^{15}\text{cm}^{-2}$), respectively, at $D = (50, 150)\text{km/s}$.

Figure 10 shows the redshift evolution of $N_{co,tot}/N_{tot}$ at $\Delta r = 100h^{-1}$ kpc in proper units, for four cases with (N_{HI}, D) of $(3 \times 10^{13}, 150)$, $(3 \times 10^{13}, 50)$, $(3 \times 10^{14}, 150)$, $(3 \times 10^{14}, 50)$. The indicated neutral hydrogen column densities in Figure 9 are approximately computed as follows. Combining Equation (2) for N_{HI} at $z = 3$ (with the adopted fiducial values of various quantities) with the result that the physical sizes of clouds go roughly as $(1+z)^{-3/2}$ (Figure 4) gives $N_{HI}(\rho_{cut}, z) = 1.0 \times 10^{13} \left(\frac{\rho_b}{3.0}\right)^2 (1+z)^{9/2} \text{cm}^{-2}$. We see that, *at a fixed column density*, the rate of coincident lines (at $\Delta r = 100$ km/s) *increases with redshift at a moderate pace*, and higher column density clouds and/or smaller D yield weaker evolution, assuming that j_{HI} is *constant* over the redshift range in question. The assumption of constant j_{HI} is merely for the convenience of illustration. In fact, the self-consistently produced photoionization field during the simulation is constant from $z = 4$ to $z = 2$ to within a factor of two. In other words, the results would not have significantly differed if the actual photoionization field had been used.

Given the three dimensional nature of the simulations, we can distinguish between two kinds of coincident lines: one of which ($N_{co,common}$) occurs when a pair shares the same 3-d parent cloud, the other of which ($N_{co,clustering}$) occurs when the lines intersect two separate 3-d clouds. The former set of coincident lines is due to the extended size of a

single cloud, while the latter set of coincident lines is due to the clustering of several clouds. Figure 11 shows $N_{co,common}/N_{co,tot}$ at $z = 3$. Six curves are shown for $\rho_{cut} = (3, 10, 30)$ with $D = 50$ km/s and 150 km/s. We see that at $\Delta r \approx 30 - 60h^{-1}\text{kpc}$ about half of the coincident line pairs share the same clouds and the other half pierce separate clouds. At $\Delta r = 100h^{-1}\text{kpc}$ only 10-20% of the total coincident line pairs share the same clouds, i.e., clustering of separate clouds dominates the coincident events at this and larger separations.

The observational signature of clustering dominated coincident lines is that the difference in line of sight velocity between the two absorption lines should be a weak function of the separation perpendicular to the line of sight. Figure 12 shows rms velocity difference of coincident line pairs along the line of sight, $R_{||,rms}$, as a function of the perpendicular separation, Δr , for $D = 50$ km/s and 150 km/s at $\rho_{cut} = (3, 10, 30)$. The two long-dashed horizontal lines show the rms difference for the two D values, if clouds are small (compared to perpendicular separation) and randomly distributed (i.e., no clustering). We see that $R_{||,rms}$ depends rather weakly on Δr when $\Delta r \geq 200h^{-1}\text{kpc}$, and it approaches the asymptotic limit of a random distribution of clouds at $\Delta r \approx 400 - 500h^{-1}\text{kpc}$. We predict that for quasar double sightlines at large separations ($\Delta r > 500h^{-1}\text{kpc}$), the rms velocity difference between absorption features common to both sightlines, $R_{||,rms}$, should depend on the range being searched in z -space, D , as

$$R_{||,rms} = 0.58D. \quad (7)$$

Figures (13a,b) show the redshift evolution of $N_{co,common}/N_{co,tot}$ for $N_{HI} = 3 \times 10^{13}\text{cm}^{-2}$ and $N_{HI} = 3 \times 10^{14}\text{cm}^{-2}$, respectively. Four cases are shown in each figure with two separations, $\Delta r = 50h^{-1}\text{kpc}$ and $\Delta r = 100h^{-1}\text{kpc}$ both in proper units, and with $D = 50\text{km/s}$ and 150km/s . We see that the fraction of coincident lines with a separation of $50 - 100h^{-1}$ proper kpc due to common clouds *decreases with increasing redshift at fixed column density*, presumably because clouds are smaller and more crowded at high redshift

than at low redshift. We remind the reader that the total line coincident rate *increases with redshift* (see Figure 10), indicates that a higher cloud number density (crowding of clouds) at high redshift dominates the line coincident events. This is consistent with results shown in Figure 11.

The combined results of our quasar double sightline analysis suggest a few basic trends which should be kept in mind when analyzing QSO spectra. The most important of these is that line coincident events can be caused by two different phenomena. At small perpendicular separations ($\Delta r < 40h^{-1}\text{kpc}$ proper) a pair of coincident lines is most likely to pierce a common cloud, as is usually assumed when analyzing such observations to infer the actual cloud size. However, at larger Δr , a pair of coincident lines is more likely to penetrate two different clouds which are spatially clustered. At $\Delta r = 100h^{-1}\text{kpc}$, only 10-20% of the total coincident line pairs share the same clouds. And at very large separations of $\Delta r > 500h^{-1}\text{kpc}$, the coincident line events can be explained as the random intersection of two unrelated clouds, whose rms difference $R_{||,rms}$ should relate to the velocity interval D as indicated in Equation (7).

3.2.5. Correlations of Ly α Clouds

It is tempting to make a connection between Ly α clouds and dwarf galaxies and/or moderate redshift faint blue galaxies. We approach this problem by examining clustering properties of the Ly α clouds.

A few cautionary words about the limitations of the simulation are in order here. The simulation box size ($L = 10h^{-1}\text{Mpc}$ comoving) places severe limits on our ability to study the clustering properties of clouds on large scales with a high degree of accuracy, because it sets an upper limit on the scale of the input power spectrum. Waves longer than the

simulation box size would have made a considerable contribution to clustering on larger scales, since the density fluctuations on scales comparable to the simulation box length have started to approach nonlinearity even at redshift $z = 2$ ($\sigma \sim 0.4$ at $z = 2$ on the box scale). The situation becomes even more serious at lower redshift.

Nevertheless, we may gain some insight into the distribution of mass on smaller scales, and say something useful about the more local clustering properties of clouds. The three dimensional correlation of the Ly α clouds at $z = 3$ is shown in Figure 14 for $\rho_{cut} = (10, 30)$. Higher column density clouds seem to be more strongly clustered than lower column density ones. Since most of the faint blue galaxies are thought to be in the redshift $z \sim 0.5 - 1.0$, we show in Figure 15 the evolution of correlation length r_o (solid curve). This is defined as the length where the correlation is unity and is plotted for the redshift range $z = 2 - 4$, where we have the most confidence in the accuracy of the simulation. All lengths are shown in comoving units.

In order to estimate the effect of missing power at box-sized scales, we computed the correlation function of the clouds in eight subboxes. These subboxes were created by dividing the original simulation box into eight equal cubes and pretending that each subbox also has periodic boundary conditions. The dotted line in Figure 15 shows the median value of the correlation length for the subboxes, and the vertical bars indicate the full width of the distribution at each redshift (i.e., highest and lowest values of r_o). We see that the median correlation length drops about 30-40% for a box of size $L = 5h^{-1}\text{Mpc}$. Our best estimate is that the true correlation length at each redshift would be larger than values indicated by the solid curves by perhaps 50%, were the simulation box sufficiently large.

Simple extrapolation of the solid curve in Figure 15 to lower redshifts is unlikely to give us accurate values of r_o at $z \sim 0.5 - 1.0$. However, it is reasonable to expect the value of r_o at these redshifts to be significantly larger than $1.5h^{-1}\text{Mpc}$ comoving, when one takes

into account the effect of the missing longer waves. This correlation length is interestingly close to the observed correlation length of the faint blue galaxies (Efstathiou et al. 1991; Neuschafer, Windhorst, & Dressler 1991; Couch, Jurcevic, & Boyle 1993; Roche et al. 1993; Infante & Pritchett 1995; Brainerd, Smail, & Mould 1995), although an accurate conversion from observed angular correlation function $\omega(\theta)$ to the 3-d correlation function as computed here requires detailed knowledge of the redshift distribution of the observed faint blue objects, which is currently unavailable. Furthermore, the average mass of these objects is close to $10^9 - 10^{10} M_\odot$ (see Table 1), which is in accord with what the mass of the faint blue galaxies is thought to be or required [cf. , e.g., Babul & Rees' (1992) starburst dwarf galaxy model]. Finally, the number density of the clouds (with a mean separation of $\sim 2h^{-1}\text{Mpc}$ at $z=2$ for $\rho_{cut} = 30$) and its increasing trend with redshift indicate that it is probably quite close to what is thought to be for observed faint blue objects. These three considerations lend tentative support to the conjecture that the high redshift Ly α clouds ($N_{HI} \geq 10^{15}\text{cm}^{-2}$) are the progenitors of the faint blue galaxies.

4. Conclusions

We have presented a quantitative study of the sizes, shapes, and correlations of Ly α clouds in a spatially flat cold dark matter universe with a cosmological constant, utilizing state-of-art cosmological hydrodynamic simulations including detailed atomic physics for a plasma of primordial composition. Keeping in mind the unavoidable limitations of such numerical experiments due to limited boxsize and limited resolution as well as some approximate treatment of physical processes, a few findings are probably fairly reliable.

Structures formed at high redshift $z \sim 2 - 4$ due to gravitational growth/collapse of cosmic density perturbations at small-to-intermediate scales (100kpc to a few Mpc comoving) are responsible for the observed Ly α forest. These Ly α clouds cannot be

described by a simple model which characterizes their sizes and shapes. Their sizes vary in a wide range from a few kiloparsecs to about one hundred kiloparsecs in proper units with the median size being $\sim 15 - 35 h^{-1} \text{kpc}$ at $z = 3$, and their shapes vary from nearly-spherical ellipsoids to filaments and pancakes. A typical Ly α cloud resembles a “flattened cigar,” with an axial ratio of $\sim 1 : 2 : 4$ at column density of $10^{13} - 10^{14} \text{ cm}^{-2}$, and is either a thin cigar with an axial ratios of $(1 : 3 : 3.4)$ or near sphere with an axial ratios of $(1 : 1.3 : 1.5)$ at column density of $> 10^{15} \text{ cm}^{-2}$. Larger clouds are, on average, less spherical than smaller ones. The physical size of a typical cloud grows with time roughly as $(1 + z)^{-3/2}$ while its shape hardly evolves (except for the most dense regions $\rho_{cut} > 30$ where tend to be more spherical with time).

Analysis of simulated quasar double sightlines indicates that coincident absorption features observed in the two spectra can have two different causes. At small perpendicular sightline separations ($\Delta r < 40 h^{-1} \text{kpc}$ proper), a pair of coincident lines most likely represents absorption from a common cloud. This is usually assumed when analyzing such observations to infer the actual cloud size. However, at larger Δr , a pair of coincident lines most likely samples two separate clouds which belong to the same cloud cluster. In other words, clustering of separate clouds dominates the coincident events at larger double sightline separations. At $\Delta r = 100 h^{-1} \text{kpc}$, 80-90% of coincident line pairs can be explained in this fashion. At very large separations, $\Delta r > 500 h^{-1} \text{kpc}$, the coincident line events are entirely due to random intersections of two unrelated, uncorrelated clouds, whose rms velocity difference $R_{||,rms}$ should relate to the velocity interval being examined, D , as $R_{||,rms} = 0.58D$. Analyzing observed coincident absorption lines to infer the actual sizes of Ly α clouds by assuming a population of clouds with simplified geometry (e.g. spheres, disks) is reasonably accurate only when the double sightline separations are small ($\Delta r \leq 50 h^{-1} \text{kpc}$). For larger Δr , this exercise is not very meaningful. The inferred sizes are not related to true sizes of the clouds and are grossly inflated.

We attempt to make a connection between the high column density Ly α clouds ($N_{HI} \geq 10^{15}$) and the faint blue galaxies. The supportive evidence for such a conjecture is threefold. First, when extrapolated to $z \sim 0.5 - 1.0$, the correlation of the high column density Ly α clouds ($\geq 1.5h^{-1}\text{Mpc}$ comoving) is close to that of the observed faint blue galaxies (Efstathiou et al. 1991; Neuschaefer, Windhorst, & Dressler 1991; Couch, Jurcevic, & Boyle 1993; Roche et al. 1993; Infante & Pritchett 1995; Brainerd, Smail, & Mould 1995). Second, the typical mass of these objects ($10^9 - 10^{10} M_{\odot}$) is close to that of a dwarf galaxy [cf. , e.g., Babul & Rees (1992) scenario]. Finally, the number density of the clouds is reasonably close to what is observed for faint blue objects.

Finally, we caution that it may be necessary to extend the simulation’s dynamic range to 1000 – 3000 cells in each dimension, in order to have both a larger box ($L \sim 20 - 30h^{-1}\text{Mpc}$ comoving) and a finer resolution ($\Delta l \sim 10 - 20h^{-1}\text{kpc}$ comoving) to ensure both a “fair” sample and fully resolved structures of the objects in question, while maintaining a sufficient mass resolution.

The work is supported in part by grants NAG5-2759, AST91-08103 and ASC93-18185. We thank the referee, George Efstathiou, for a constructive and pertinent report which improved the quality of the work. Discussions with J.R. Gott, N. Katz, G. Lake, J. Miralda-Escudé and J.P. Ostriker are gratefully acknowledged. RC would like to thank G. Lake and Department of Astronomy of University of Washington for the warm hospitality, and financial support from the NASA HPCC/ESS Program during a visit when much of this work was completed.

REFERENCES

Adams, F., Bond, J.R., Freese, K., Frieman, J. & Olinto, A., 1993, preprint

Babul, A., & Rees, M. 1992, MNRAS, 255, 346

Bahcall, N., & Cen, R. 1992, *Astrophys. Lett.*, 407, L49

Bahcall, N.A., & Cen, R. 1993, *Astrophys. Lett.*, 407, L49

Bechtold, J., Crotts, A.P.S., Duncan, R.C., Fang, Y. 1994, *ApJ*, 437, L83

Bechtold, J., & Yee, H.K.C. 1996, *ApJ*, in press

Bertschinger, E., & Gelb, J.M. 1991, *Comp. Phys.*, 5, 164

Bolte, M., & Hogan, C.J. 1995, *Nature*, 376, 399

Bond, J.R., Myers, 1996, *ApJ*,

Brainerd, T.G., Smail, I., & Mould, J. 1995, preprint

Bucher, Goldhaber, & Turok, N. 1995, preprint

Carswell, R. F., Lanzetta, K. M., Parnell, H. C., & Webb, J. K., 1991, *ApJ*, 371, 36

Cen, R. 1992, *ApJS*, 78, 341

Cen, R., & Ostriker, J.P. 1993a, *ApJ*, 417, 404

Cen, R., & Ostriker, J.P. 1993b, *ApJ*, 417, 415

Cen, R., & Ostriker, J.P. 1994, *ApJ*, 431, 451

Cen, R., Gnedin, N.Y., & Ostriker, J.P. 1993, *ApJ*, 417, 387

Cen, R., Gnedin, N.Y., Kofman, L.A., & Ostriker, J.P. 1992, *ApJ*, 399, L11

Cen, R., Ostriker, J.P., & Peebles, P.J.E. 1993, *ApJ*, 415, 423

Cen, R., Miralda-Escudé, J., Ostriker, J. P., & Rauch, M. 1994, *ApJ*, 437, L9

Couch, W.J., Jurcevic, J.S., & Boyle, B.J. 1993, *MNRAS*, 260, 241

Cowie, L.L., Lilly, S.J., Gardner, J.P., & McLean, I.S. 1988, *ApJ*, 332, L29

Cristiani, S., D'Odorico, S., Fontana, A., Giallongo, E., & Savaglio, S. 1995, *MNRAS*, 273, 1016

Davis, M., Summers, F.J., & Schlegel, D. 1992, *Nature*, 359, 393

Dinshaw, N., Impey, C.D., Foltz, C.B., Weymann, R.J., & Chaffee, F.H. 1994, *ApJ*, 437, L87

Dinshaw, N., Foltz, C.D., Impey, C.D., Weymann, R.J., & Morris, S.L. 1995, *Nature*, 373, 223

Edelson, & Malkan 1986, *ApJ*, 308, 59

Efstathiou, G., Bond, J.R., & White, S.D.M. 1992, *MNRAS*, 258, 1p

Efstathiou, G., Bernstein, G., Tyson, J.A., Katz, N., & Guhathakurta, P. 1991, *ApJ*, 380, L47

Eke, V.R., Cole, S., & Frenk, C.S. 1996, preprint

Fang, Y., Dunca, R.C., Croots, A.P.S., & Bechtold, J. 1996, preprint

Feldman, H.A., Kaiser, N., & Peacock, J.A. 1994, *ApJ*, 437, 56

Freedman, M.L., et al. 1994, *Nature*, 371, 757

Gott, J.R., III 1982, *Nature*, 295, 304

Hamuy, M., et al. 1995, AJ, 109, 1

Hernquist, L., Katz, N., & Weinberg, D.H. 1996, ApJ, 457, L51

Hu, E. M., Kim, T.-S., Cowie, L. L., Songaila, A., & Rauch, M. 1995, AJ, 110, 1526

Infante, L., & Pritchett, C.J. 1995, ApJ, 439, 565

Klypin, A., Holtzman, J., Primack, J., & Regos, E. 1993, ApJ, 416, 1

Kofman, L.A., Gnedin, N.Y., & Bahcall, N.A. 1993, ApJ, 413, 1

Koo, D. 1986, ApJ, 311, 651

Liddle, A.R., Lyth, D.H., & Sutherland, W. 1992, Phys. Lett., B 279, 244

Lidsey, J.E., Coles, P. 1992, MNRAS, 258, 57p

Lucchin, F., Matarrese, S., & Mollerach, S., 1993, submitted to ApJ(Letters)

Ma, C.P., & Bertschinger, E. 1994, ApJ, 435, L9

Miralda-Escudé, J., Cen, R., Ostriker, J. P., & Rauch, M. 1996, ApJ, in press

Neuschafer, L.W., Windhorst, R.A., & Dressler, A. 1991, ApJ, 382, 32

Ostriker, J.P., & Steinhardt, P. 1995, Nature, 377, 600

Oukbir, J., & Blanchard, A. 1992, A& A, 262, L21

Peacock, J.A., & Dodds, S.J. 1994, MNRAS, 267, 1020

Peebles, P.J.E. 1984, ApJ, 284, 439

Peebles, P.J.E 1987a, Nature, 327, 210

Peebles, P.J.E 1987b, ApJ, 315, L73

Pen, U.-L. 1996, in preparation

Petitjean, P., Webb, J. K., Rauch, M., Carswell, R. F., & Lanzetta, K., 1993, MNRAS, 262, 499

Rauch, M., Carswell, R. F., Chaffee, F. H., Foltz, C. B., Webb, J. K., Weymann, R. J., Bechtold, J., & Green, R. F. 1992, ApJ, 390, 387

Riess, A.G., Press, W.H., & Kirshner, R.P. 1995, ApJ, 438, L17

Roche, N., Shanks, T., Metcalfe, N., & Fong, R. 1993, MNRAS, 263, 360

Scalo, J.M. 1986, Fund. Cosmic Phys., 11, 1

Schneider, D.P., et al. 1993, ApJS, 87, 45

Smette, A., Surdej, J., Shaver, P.A., Foltz, C.B., Chaffee, F.H., Weymann, R.J., Williams, R.E., & Magain, P. 1992, ApJ, 389, 39

Smette, A., Robertson, J.G., Shaver, P.A., Reimers, D., Wisotzki, L., & Kohler, T.H. 1995, in press

Smoot, G.F., et al. 1992, Astrophys. Lett., 396, L1

Taylor, A.N., & Rowan-Robinson, M. 1992, Nature, 359, 396

Tyson, J.A. 1988, AJ, 96, 1

Tytler, D., Fan, X.-M., & Burles, S. 1996, Nature, 381, 207

Tytler, D., Fan, X.-M., Burles, S., Cottrell, L., Davis, C., Kirkman, D., & Zuo, L. 1995, in *QSO Absorption Lines*, Proc. ESO Workshop, ed. G. Meylan (Heidelberg: Springer), p. 289

Viana, P.T.P., & Liddle, A.R. 1995, preprint

Walker, T.P., Steigman, G., Schramm, D.N., Olive, K.A., & Kang, H.S. 1991, ApJ, 376, 51

White, S.D.M., Efstathiou, G., & Frenk, C.S. 1993, MNRAS, 262, 1023

White, S.D.M., Navarro, J.F., Evrard, A.E., & Frenk, C.S. 1993, Nature, 366, 429

Zhang, Y., Anninos, P., & Norman, M.L. 1995, ApJ, 453, L57

Fig. 1.— displays three dimensional isodensity surfaces at $\rho_{cut} = (3, 10, 30)$ (in panels a,b,c), respectively, at $z = 3$.

Fig. 2.— Figure 2a shows two randomly selected slices of size $5 \times 5 h^{-2} \text{Mpc}^2$ with thickness of $175 h^{-1} \text{kpc}$ at $z = 3$ (all lengths are in comoving units). The two left panels show the density contours with $\rho_{cut} 10^{(i-1)/2}$, $i = 1, 2, 3, \dots$, and the two right panels show the identified clouds in the same slices, where two symbols are used to show two types of clouds: the filled dots represent “large” clouds with their sizes roughly indicating the actual sizes of the clouds, and the open circles are for the “small” clouds (see text for definitions). Figure 2b is the same as Figure 2a but with $\rho_{cut} = 10$ for two different slices.

Fig. 3.— shows the cumulative distributions of the cloud sizes at $z = 3$ for three different cases: $\rho_{cut} = (3, 10, 30)$, weighted by A (thin curves) and by mass (thick curves).

Fig. 4.— shows the redshift evolution of the median size of the clouds weighted by A (thin curves) and by mass (thick curves). Note that here the size (vertical axis) is in comoving length units.

Fig. 5.— shows the distributions of the shapes of the clouds in the c/b - b/a plane for clouds at $z = 3$ at $\rho_{cut} = 3$ (5a), $\rho_{cut} = 10$ (5b) and $\rho_{cut} = 30$ (5c). Each dot represents one cloud and the contours indicate the density of clouds (weighted by A) in the plane. The contour levels are incremented up linearly from outside to inside. We see that the most common cloud at $\rho_{cut} = 3$ and 10 is an ellipsoid with axial ratio of $\sim 1 : 2 : 4$. At $\rho = 30$ there are two major concentrations of clouds at $(b/a, c/b) = (0.35, 0.85)$ and $(0.75, 0.85)$, indicating the existence of two distinct populations: filaments and near-spherical ellipsoids.

Fig. 6.— shows the shape η as a function of size S at $z = 3$ for $\rho_{cut} = (3, 10, 30)$ (from top panel to bottom panel), respectively. There is a trend, with large scatters, that larger clouds tend to be less spherical and more filamentary.

Fig. 7.— represents the A -weighted cumulative distribution of η for three cases at $z = 3$.

Fig. 8.— shows the redshift evolution of the median shape parameter η_{med} .

Fig. 9.— shows the fraction of lines which are coincident at $z = 3$, $N_{co,tot}/N_{tot}$ (where $N_{co,tot} = N_{co,common} + N_{co,clustering}$), as a function of Δr . Six curves are shown for three values of $\rho = (3, 10, 30)$ each at two values of $D = (50, 150)$ km/s.

Fig. 10.— shows the redshift evolution of $N_{co,tot}/N_{tot}$ at $\Delta r = 100h^{-1}$ kpc in proper units, for four cases with (N_{HI}, D) of $(3 \times 10^{13}, 150)$, $(3 \times 10^{13}, 50)$, $(3 \times 10^{14}, 150)$, $(3 \times 10^{14}, 50)$.

Fig. 11.— shows the ratio of coincident line pairs, each of which shares the same cloud, to the total number of coincident line pairs, $N_{co,common}/N_{co,tot}$, at $z = 3$. Six curves are shown for $\rho = (3, 10, 30)$ with $D = 50$ km/s and 150 km/s.

Fig. 12.— shows rms difference of coincident line pairs along the line of sight, $R_{||,rms}$, as a function of the sightline separation perpendicular to the line of sight, Δr , for $D = 50$ km/s and 150 km/s at $\rho_{cut} = (3, 10, 30)$. Also shown as the two long-dashed horizontal lines are the rms separations for the two D values, if clouds are small (compared to perpendicular separation) and randomly distributed.

Fig. 13.— shows the redshift evolution of $N_{co,common}/N_{co,tot}$ for $N_{HI} = 3 \times 10^{13} \text{ cm}^{-2}$ (panel a) and $N_{HI} = 3 \times 10^{14} \text{ cm}^{-2}$ (panel b), respectively. Four cases are shown in each figure with two separations, $\Delta r = 50h^{-1}$ kpc and $\Delta r = 100h^{-1}$ kpc both in proper units, and with $D = 50$ km/s and 150 km/s.

Fig. 14.— shows the correlation of Ly α clouds at $z = 3$ for $\rho_{cut} = (10, 30)$.

Fig. 15.— shows the redshift evolution of correlation length r_o (solid curve) defined as the length where correlation is unity (in comoving length units). Also shown as the dotted curve is the correlation length computed using the eight subboxes to illustrate the effect of the

simulation boxsize on the correlation.

Table 1. Cloud Statistics

Redshift	ρ_{cut}	# of Clouds	Mass fraction	$\langle r_{sp} \rangle$ (Mpc proper)	$\langle m_{cloud} \rangle$ (M $_{\odot}$)
2	3.0	2027	0.51	0.42	3.8×10^9
3	3.0	3025	0.43	0.26	2.1×10^9
4	3.0	3955	0.36	0.20	1.3×10^9
2	10.0	1191	0.33	0.49	4.1×10^9
3	10.0	1696	0.25	0.32	2.1×10^9
4	10.0	2197	0.19	0.23	1.2×10^9
2	30.0	683	0.20	0.57	4.3×10^9
3	30.0	986	0.14	0.38	2.0×10^9
4	30.0	1242	0.10	0.28	1.1×10^9

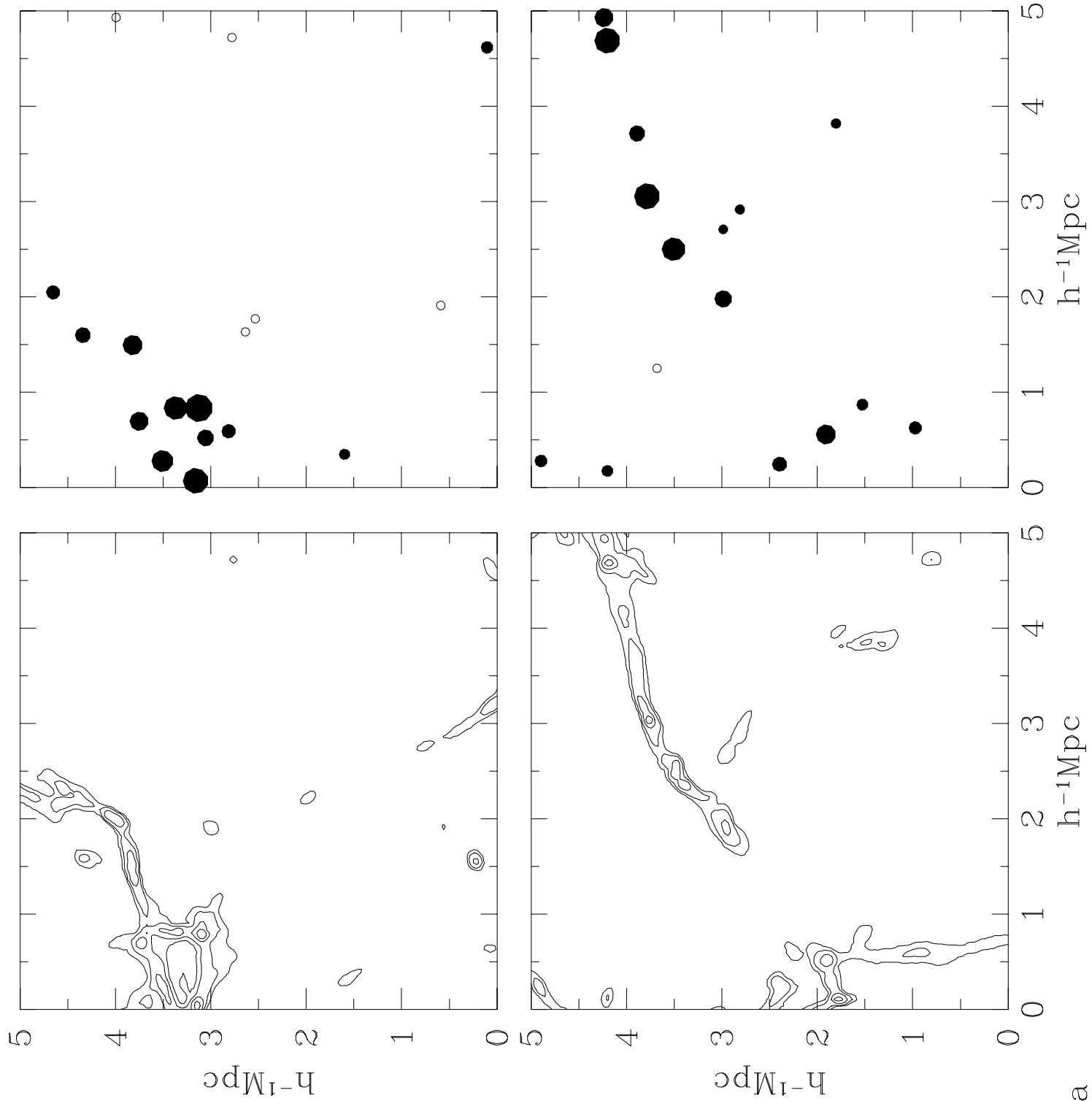


Figure 2a

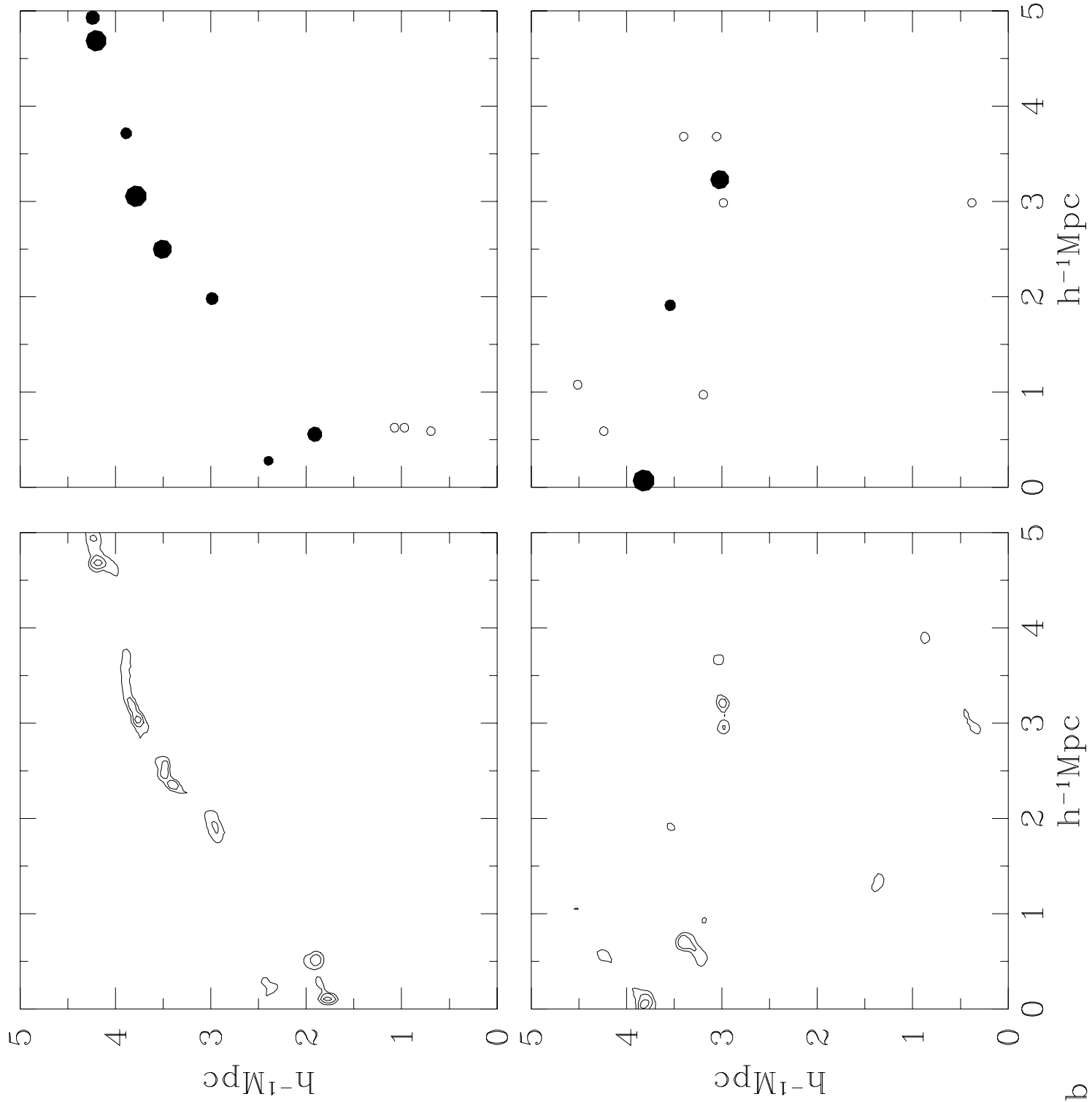


Figure 2b

Figure 3

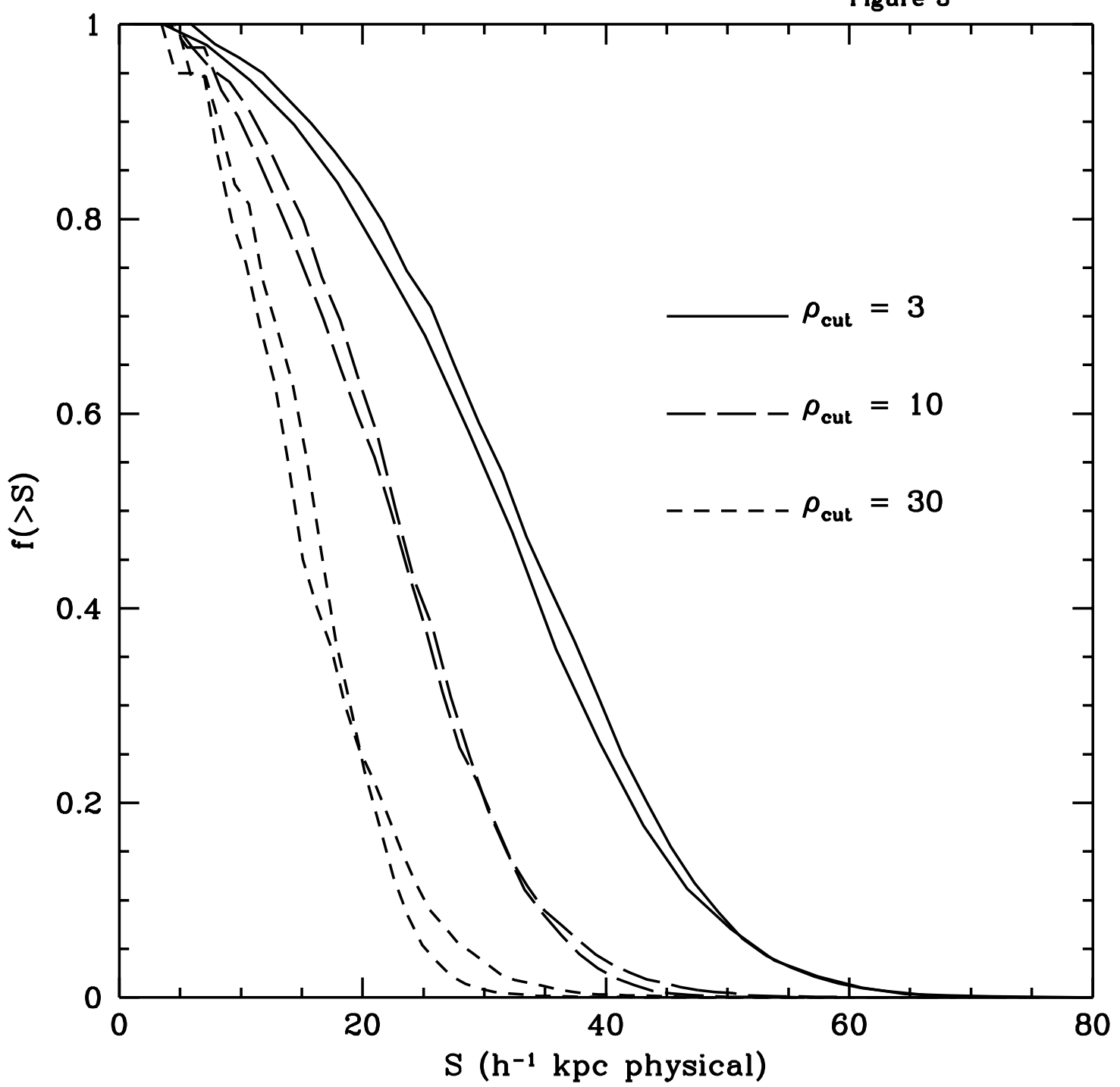


Figure 4

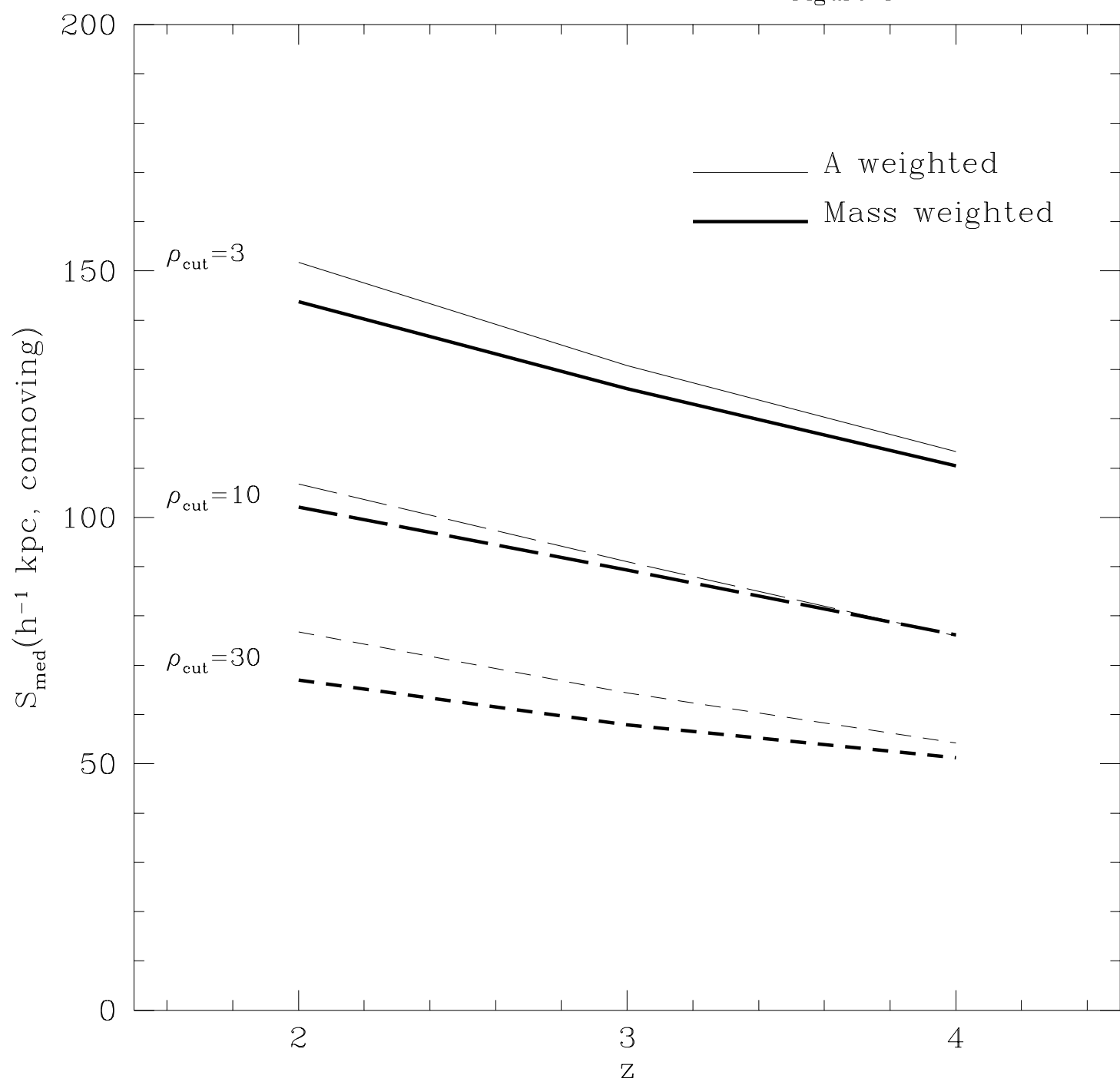


Figure 5a

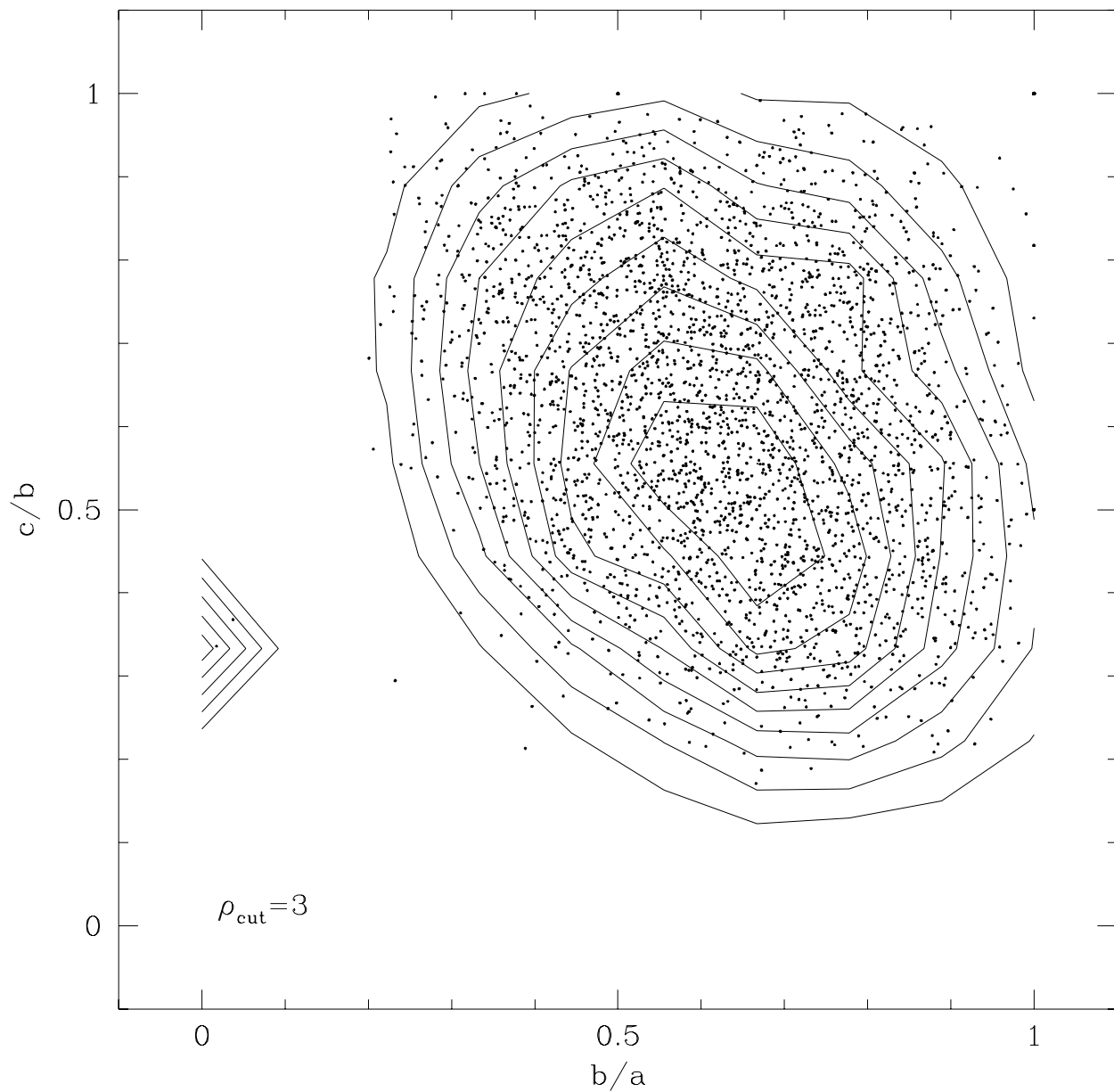


Figure 5b

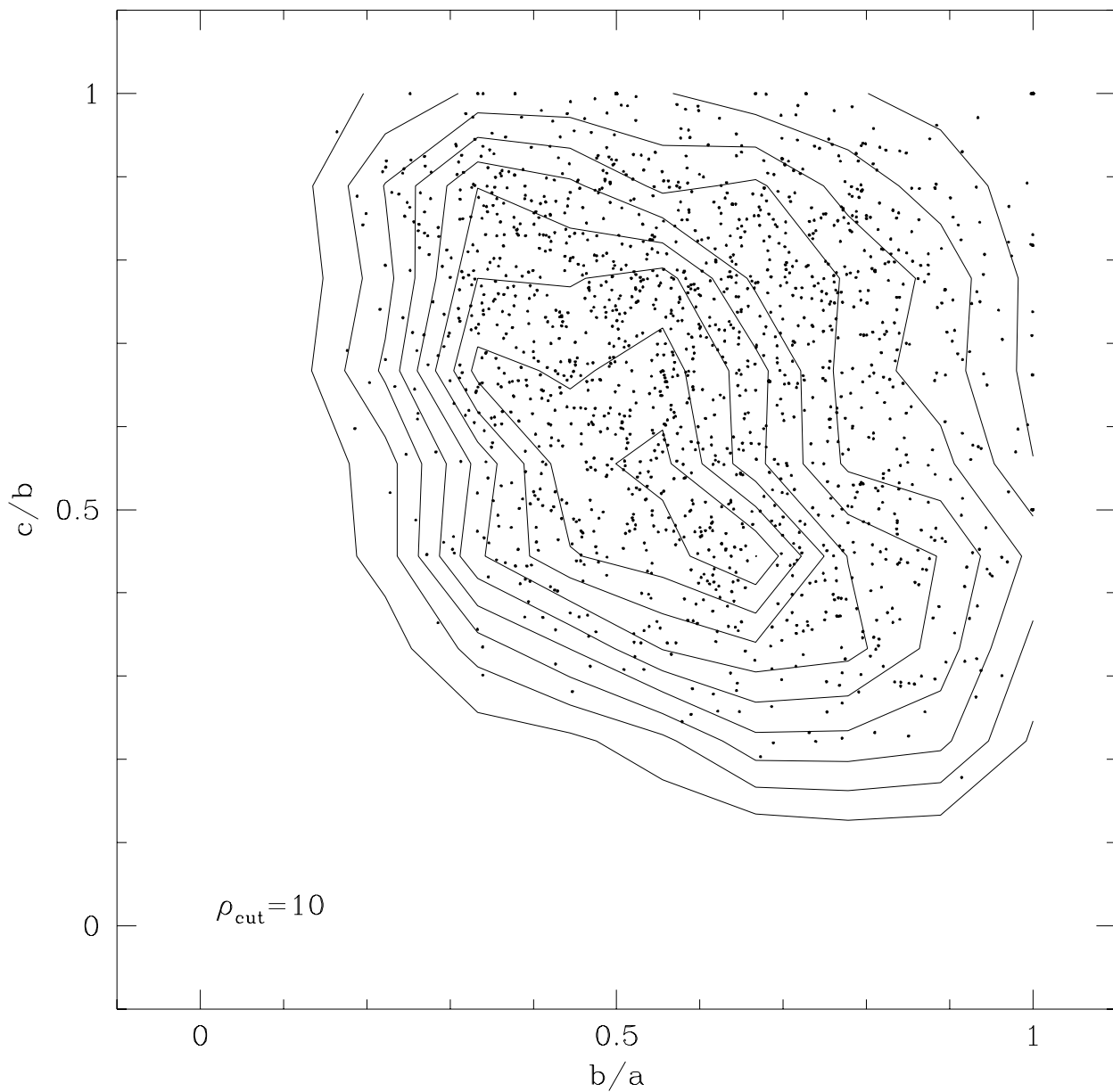


Figure 5c

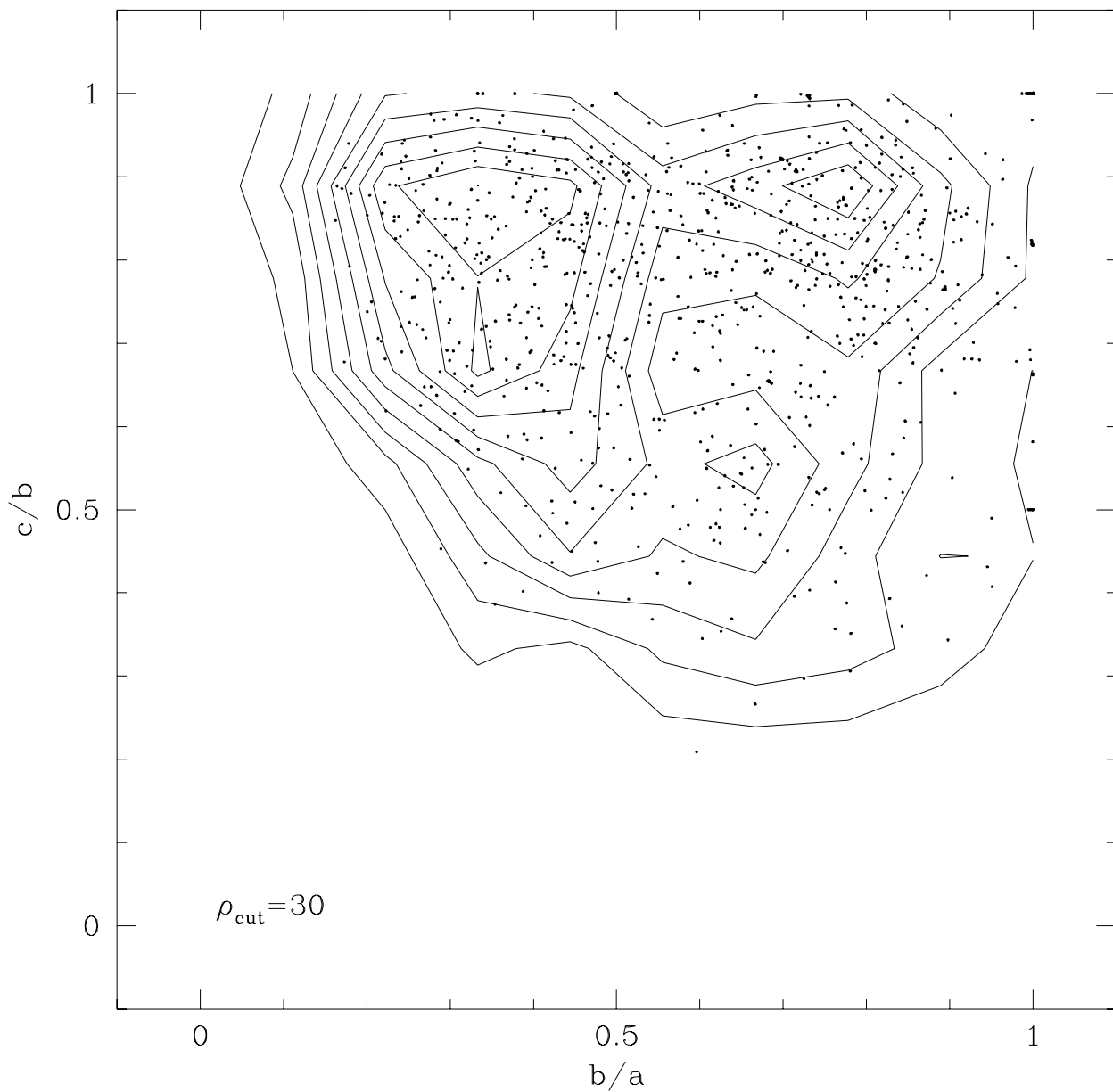


figure 6

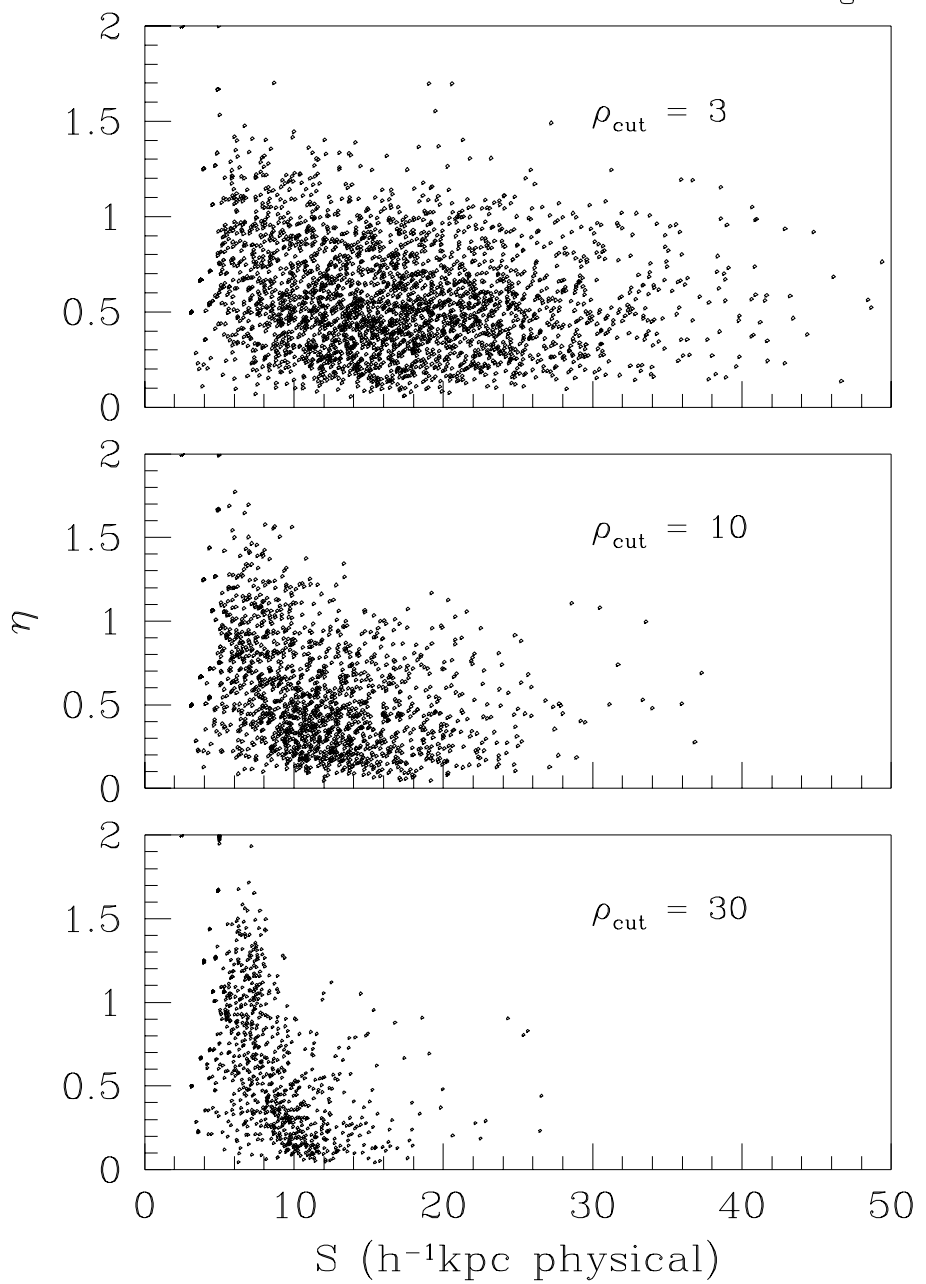


Figure 7

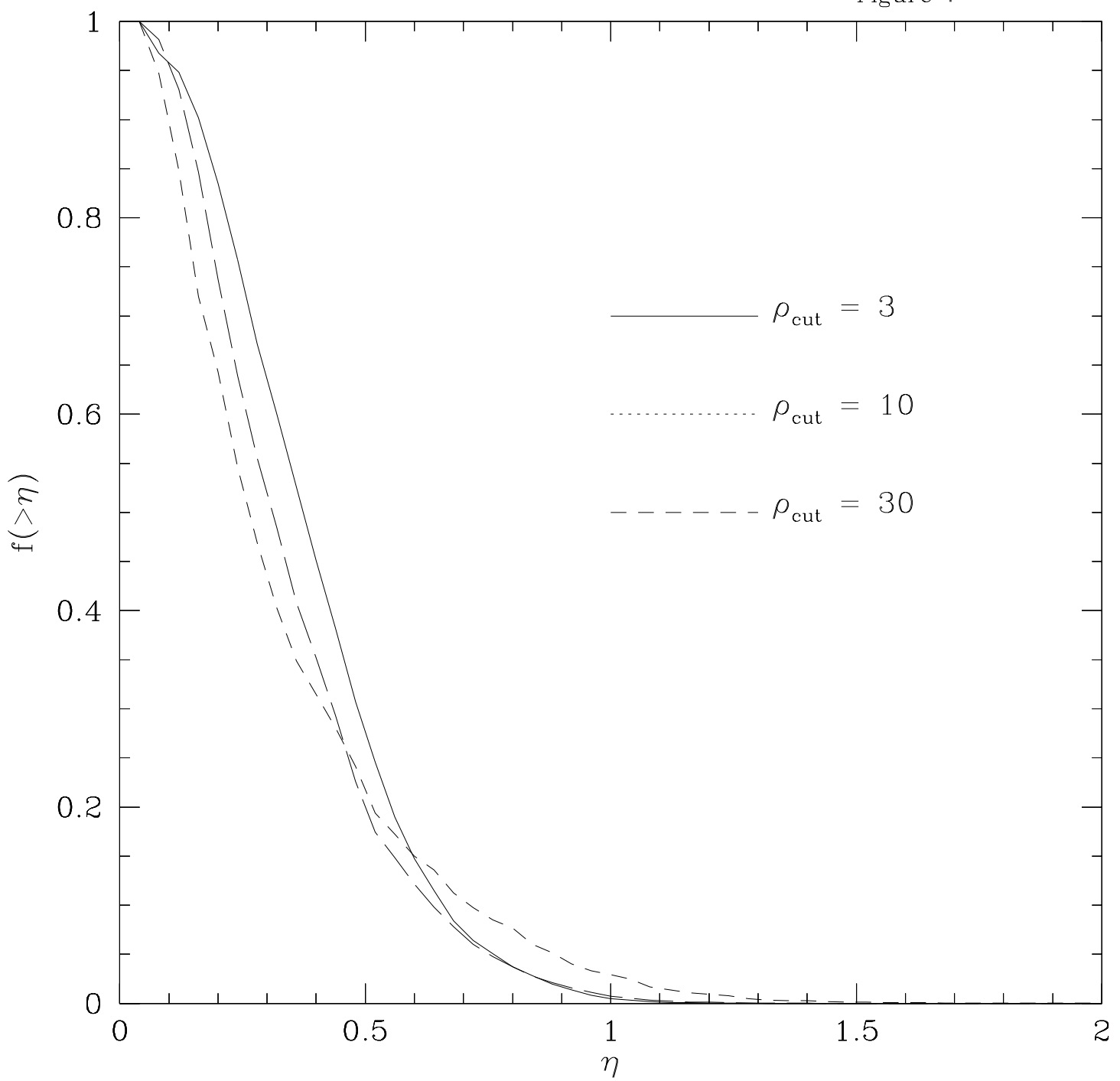


figure 8

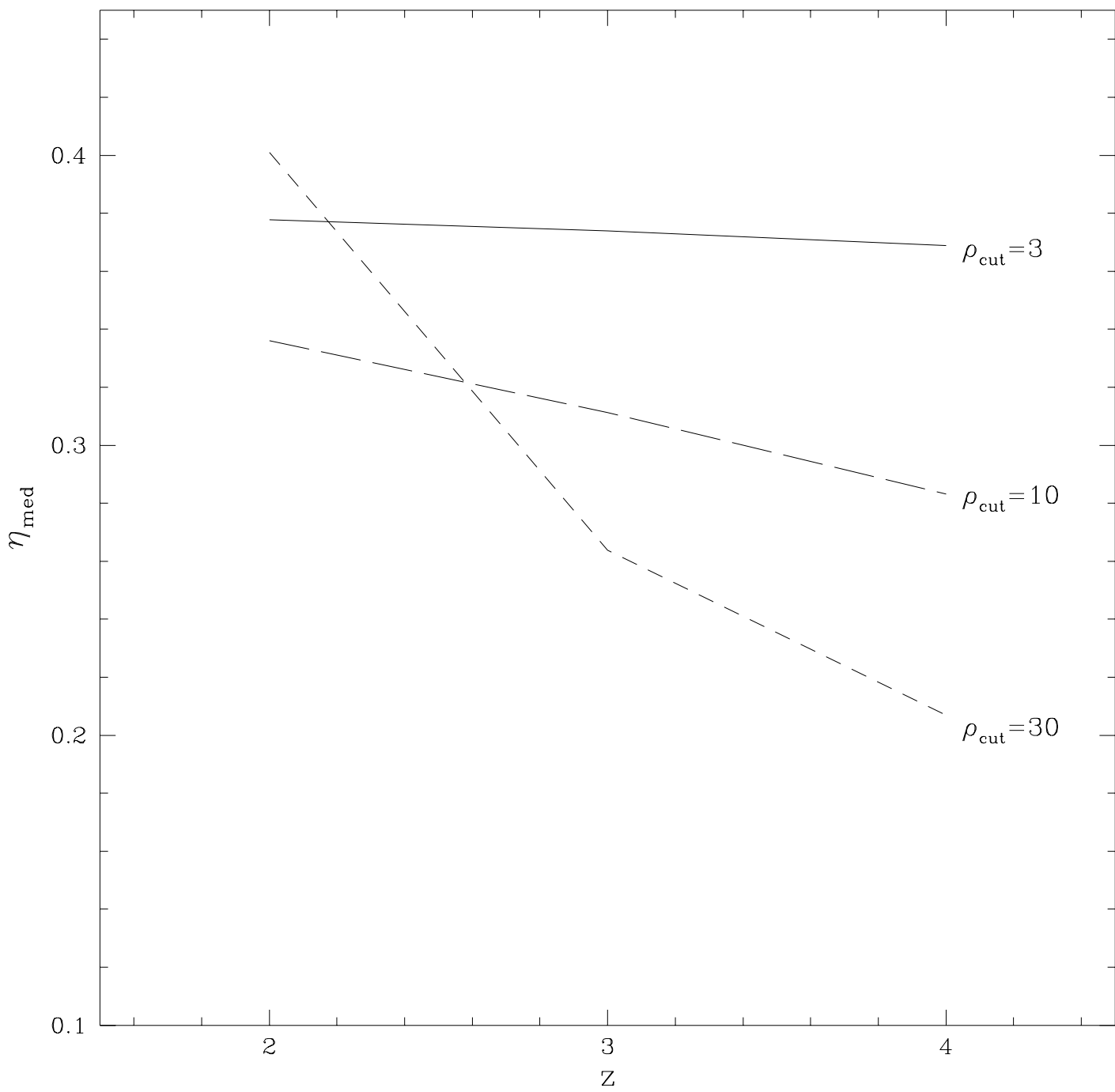


Figure 9

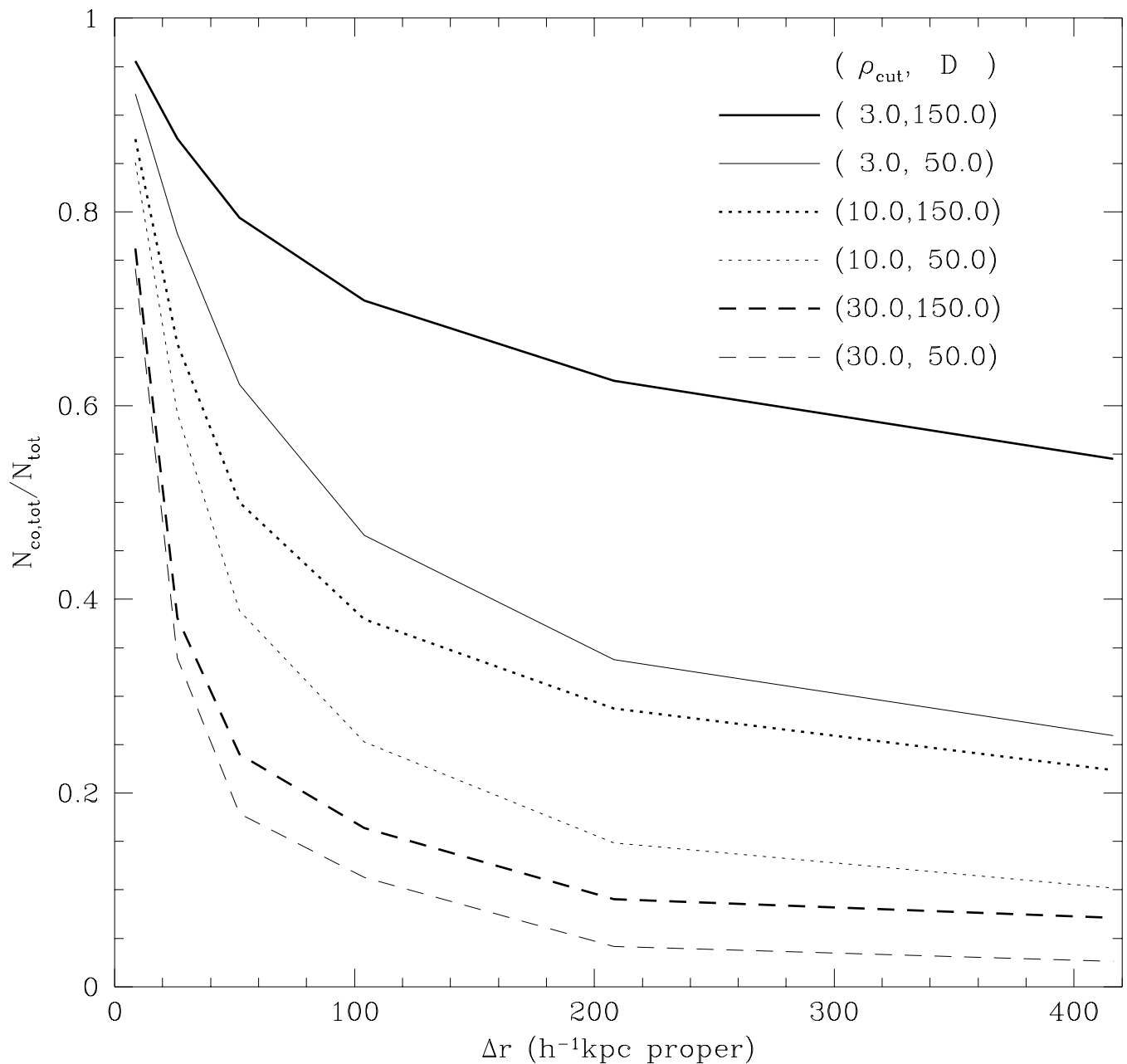


Figure 10

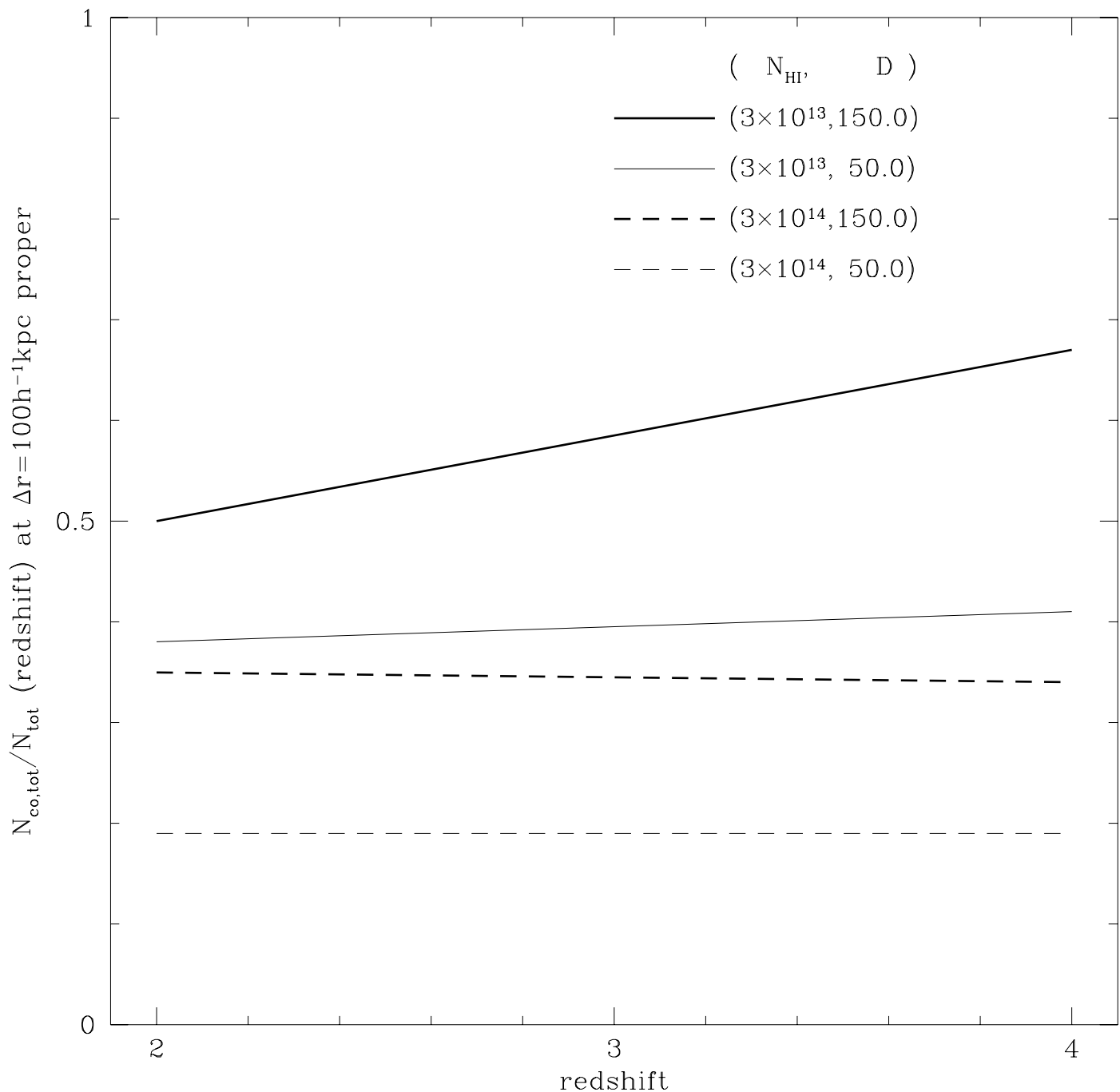


Figure 11

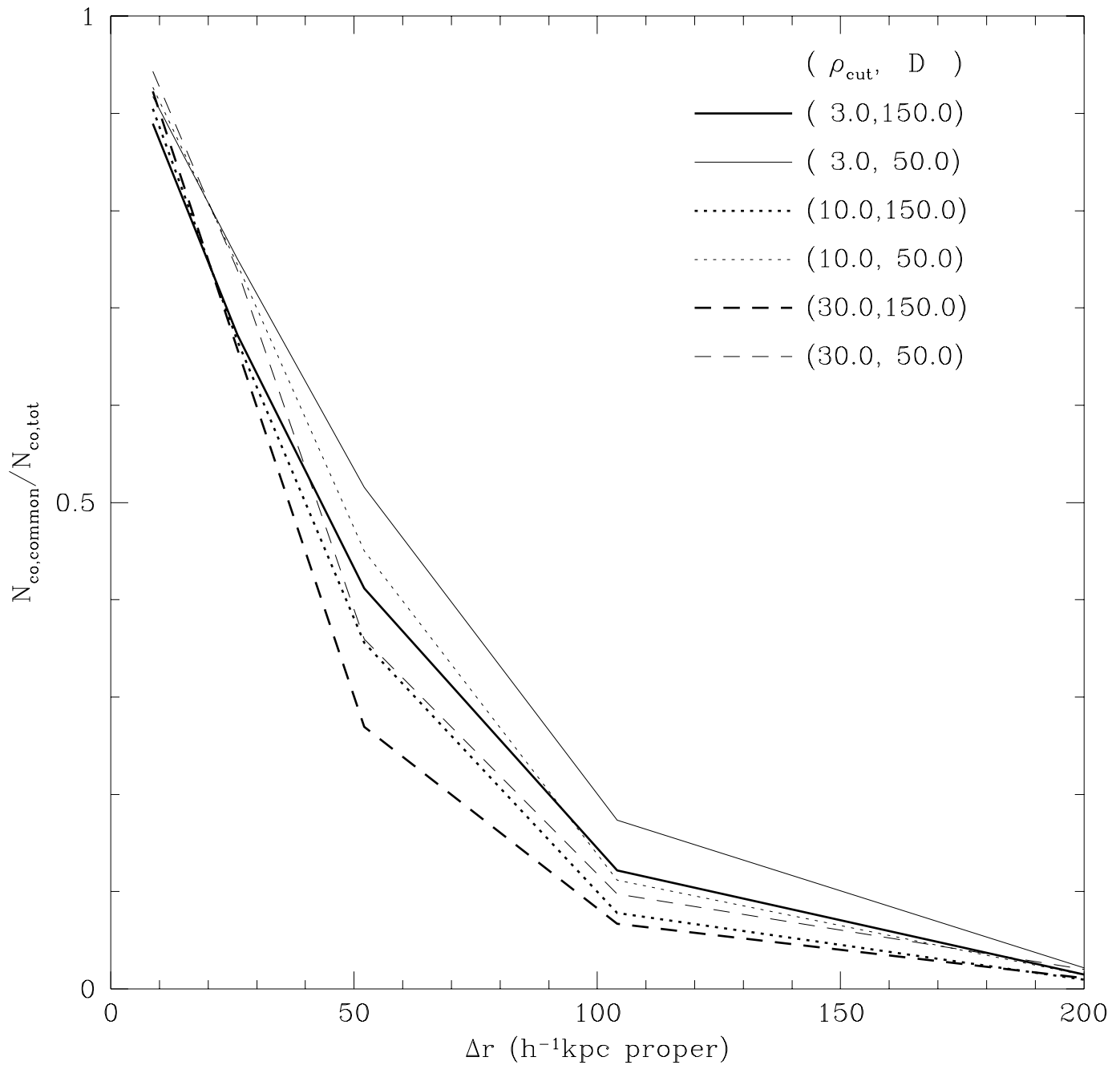


Figure 12

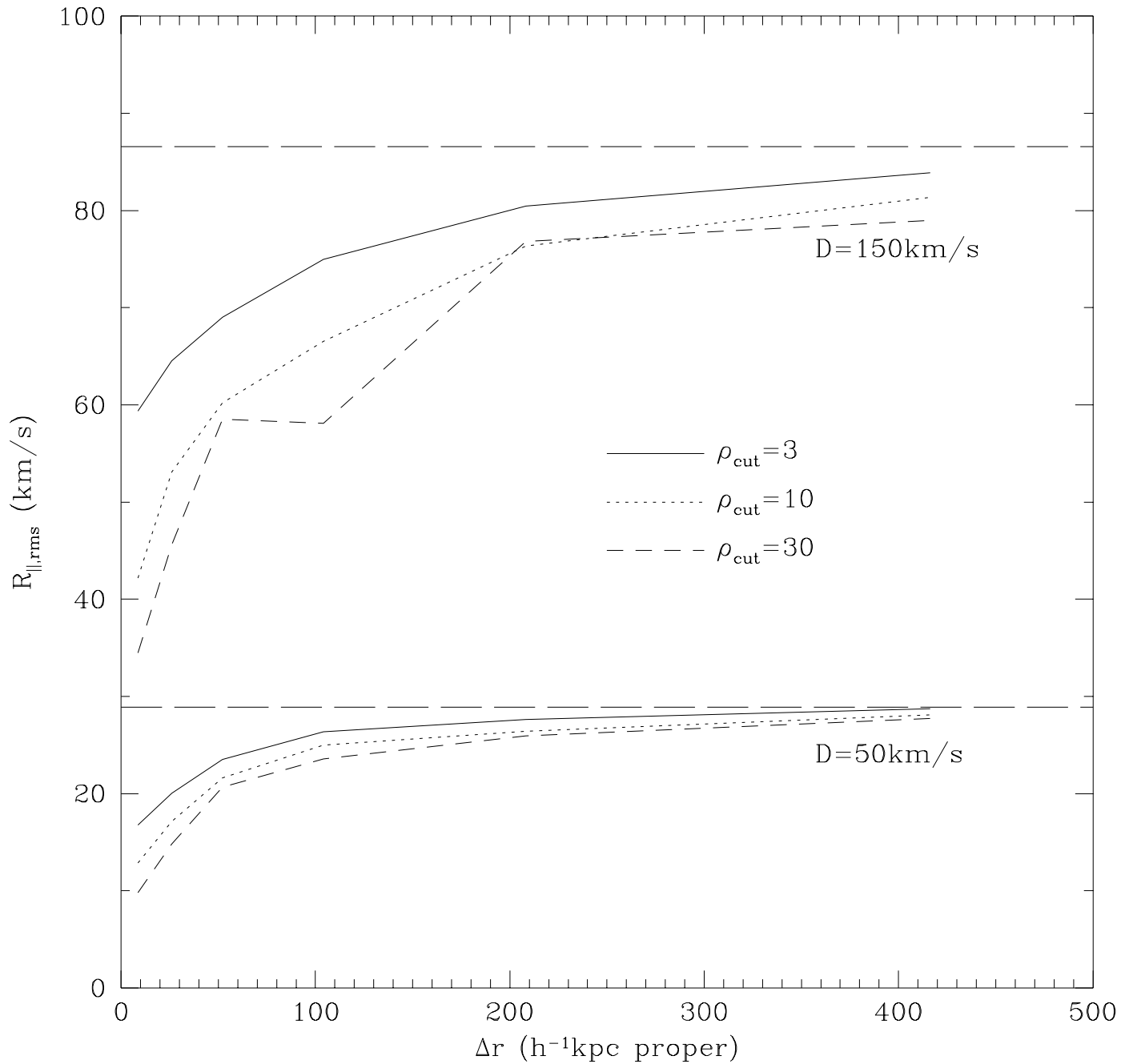


Figure 13a

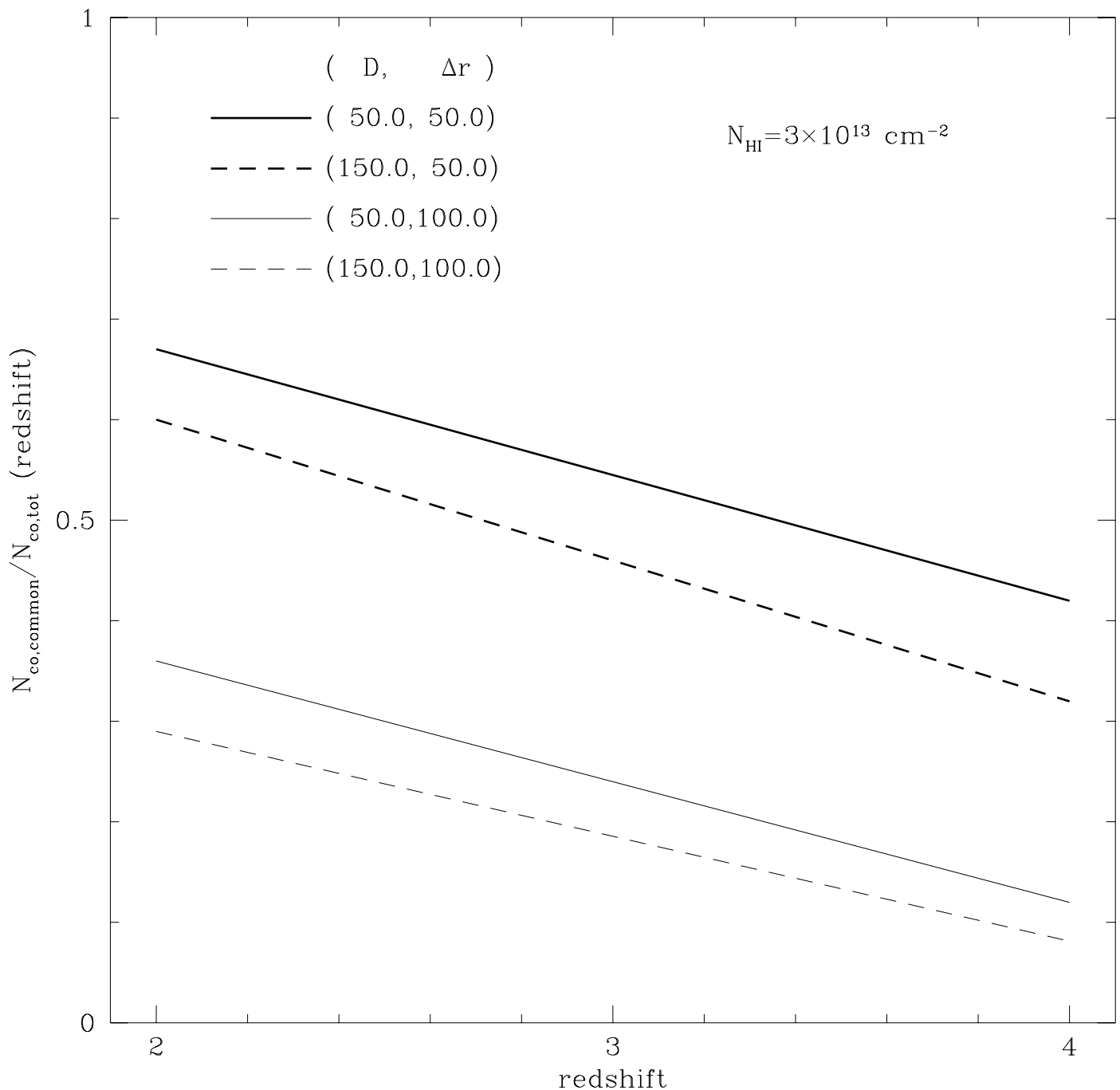


Figure 13b

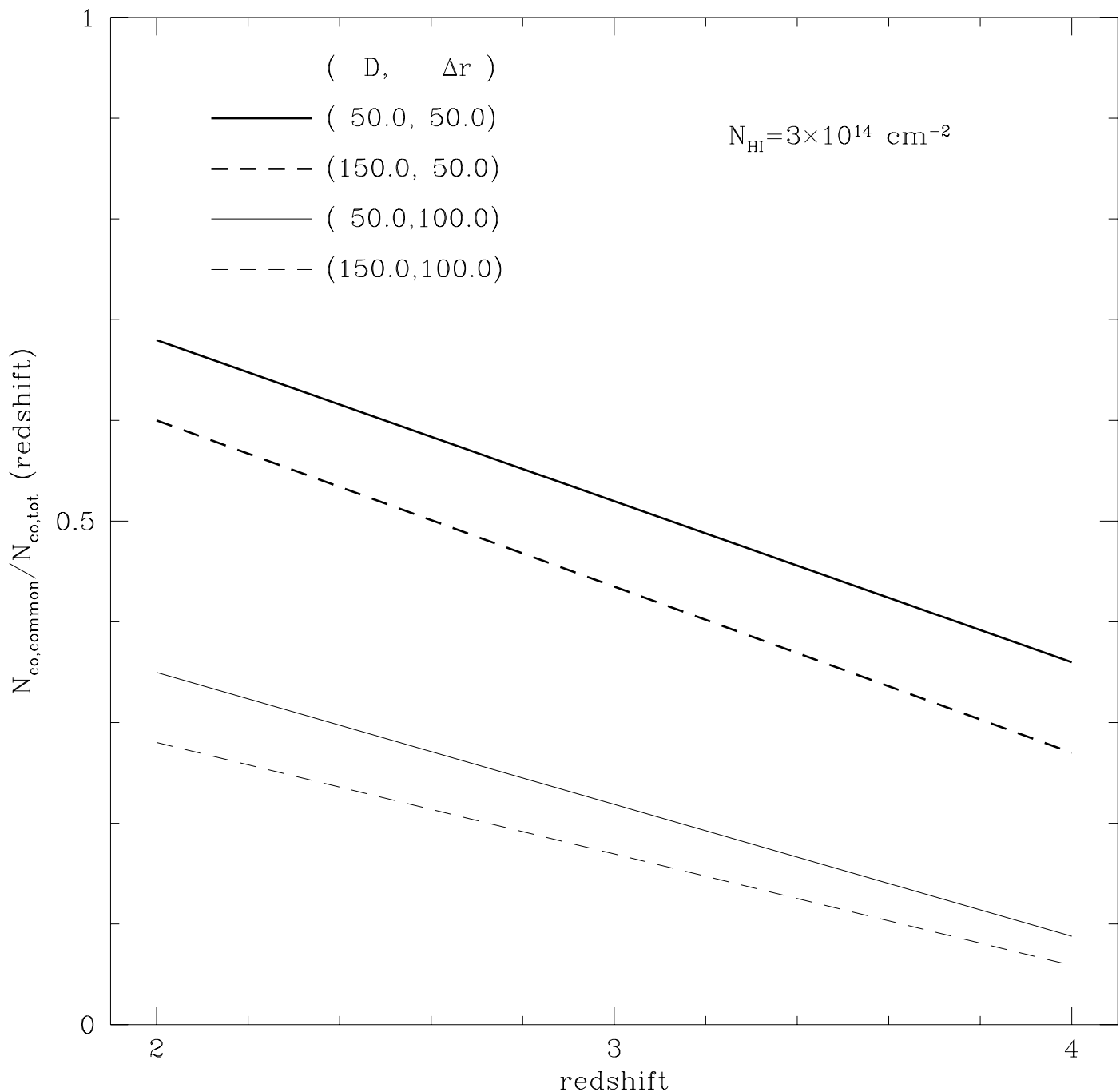


figure 14

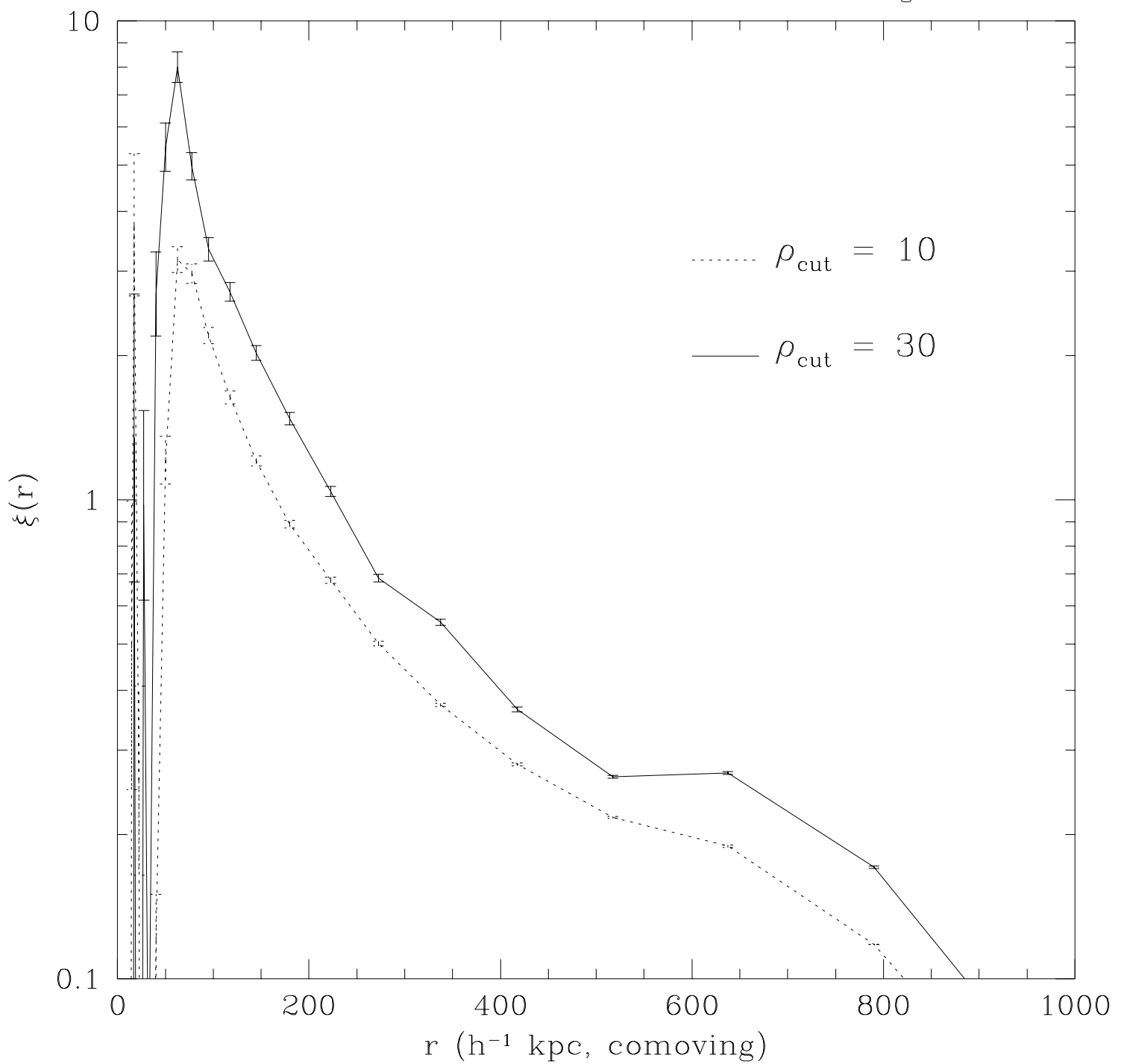


figure 15

